

Improved near surface continental climate in IPSL-CM6A-LR by combined evolutions of atmospheric and land surface physics

Frédérique Cheruy¹, Agnès Ducharne², Frédéric Hourdin¹, Ionela Musat¹,
Etienne Vignon³, Guillaume Gastineau⁴, Vladislav Bastrikov⁵, Nicolas
Vuichard⁵, Binta Diallo¹, Jean-Louis Dufresne¹, Josefine Ghattas⁶, Jean-Yves
Grandpeix¹, Abderrahmane Idelkadi¹, Lidia Mellul¹, Fabienne Maignan⁵,
Martin Menegoz⁷, Catherine Ottlé⁵, Philippe Peylin⁵, Jérôme Servonnat⁵,
Fuxing Wang¹, Yanfeng Zhao¹

¹Laboratoire de Météorologie Dynamique/IPSL/Sorbonne Universités/CNRS, UMR 8539, 4 pl Jussieu,
Paris, 75005, France.

²Sorbonne Université, CNRS, EPHE, Milieux environnementaux, transferts et interaction dans les
hydrosystèmes et les sols, Metis, 75005 Paris, France

³Environmental Remote Sensing Laboratory, Ecole Polytechnique Fédérale de Lausanne (EPFL),
Switzerland

⁴Locean/IPSL/Sorbonne Universités/CNRS

⁵Institut Pierre Simon Laplace, IPSL/SU

⁶Laboratoire des Sciences du Climat et de l'Environnement, IPSL, unité mixte CEA-CNRS-UPS, Gif sur
Yvette, France.

⁷Institut des Goscience de l'Environnement (IGE), Université Grenoble Alpes

Key Points:

- The representation of the land-atmosphere coupled system by the IPSL model is thoroughly evaluated.
- Improvements with respect to previous versions are documented in the context of the Coupled Model Intercomparison Project, CMIP.
- Advanced parameterization of land surface and atmospheric processes, tuning of the radiation and the turbulent mixing yielded many improvements.

Corresponding author: Frédéric Cheruy, frederique.cheruy@lmd.jussieu.fr

28 **Abstract**

29 This work is motivated by the identification of the land-atmosphere interactions
 30 as one of the key sources of uncertainty in climate change simulations. It documents new
 31 developments in related processes, namely boundary layer/convection/clouds parame-
 32 terizations and land surface parameterization in the Earth System Model of the Insti-
 33 tut Pierre Simon Laplace (IPSL). Simulations forced by Sea Surface Temperature are
 34 produced with different combinations of atmospheric and land surface parameterizations.
 35 They are used to explore the sensitivity to the atmospheric physics and/or soil physics
 36 of

- 37 • major bias in the near surface variables over continents,
- 38 • the energy and moisture coupling established at the soil/atmosphere interface in
 39 not too wet (energy limited) and not too dry (moisture limited) soil moisture (SM)
 40 regions also known as transition or "hot-spot" regions
- 41 • the river runoff at the outlet of major rivers.

42 The package implemented in the IPSL-Climate Model (CM) for the phase 6 of the Cou-
 43 pled Models Intercomparison Project (CMIP6) allows to reduce several biases in the sur-
 44 face albedo, the snow cover and the continental surface air temperature in summer as
 45 well as in the temperature profile in the surface layer of the polar regions. The interac-
 46 tions between soil moisture and atmosphere in hot-spot regions are in better agreement
 47 with the observations. Rainfall is also significantly improved in volume and seasonality
 48 in several major river basins leading to an overall improvement in river discharge. How-
 49 ever, the lack of consideration of floodplains and human influences in the model, e.g. dams,
 50 irrigation, impacts the realism of simulated discharge.

51 **Plain Language Summary**

52 Land surface-atmosphere interactions play an essential role in the climate system.
 53 They strongly modulate the regional climates and have impacts on the global scale for
 54 instance through freshwater release into the oceans. Climate hazards (heat waves, drought)
 55 and their impacts on populations also strongly depend on interactions between land and
 56 atmosphere and on their evolution with climate change. Climate models are precious tools
 57 to investigate how the Earth climate behaves. The 6th phase of the Climate Model In-
 58 tercomparison Project (CMIP6) provides important tools to measure the progress and
 59 address the remaining open questions regarding the continental climate modeling. The
 60 representation of the land-atmosphere coupled system by the IPSL-Climate Model (CM)
 61 involved in CMIP6 is thoroughly evaluated against observations and compared with sim-
 62 ulations using the CMIP5 version. Several biases concerning the temperature over land
 63 and over the ice sheets, and with the snow cover are significantly reduced. Numerous im-
 64 provements were made developping advanced parameterizations and tuning of the ra-
 65 diation and of the turbulent mixing in the atmospheric model. The realism of the sea-
 66 sonal cycle of hydrological variables such as the precipitation or the river discharge is
 67 also improved over many regions. The new treatment of hydrology paves the way for fu-
 68 ture developments on water resource aspects in the climate model.

69 **1 Introduction**

70 Earth's climate and its evolution are determined by interactions between the ocean,
 71 the atmosphere, ice caps and land surfaces under the external solar forcing and the at-
 72 mospheric composition. For these reasons, numerical models need to couple all these com-
 73 ponents of the system when they are used for running climate projections to anticipate
 74 the impacts of climate change. In this general framework, the land surface-atmosphere

75 interactions strongly modulate the regional climate (e.g. S. I. Seneviratne et al., 2010),
76 they particularly control climate hazards and their consequences (Jaeger & Seneviratne,
77 2011; Miralles et al., 2014), impact the freshwater discharge into the oceans and, in turn
78 the thermohaline circulation (Peterson et al., 2002). They rely on complex overlap of mul-
79 tiple land-atmosphere feedback processes and depend on the representation of the inter-
80 actions between the soil moisture and the boundary layer through the partition of the
81 available energy at the surface in sensible and latent heat, the impact on radiation (Betts
82 et al., 1996; Eltahir, 1998; Schär et al., 1999), the representation of the convection and
83 its sensitivity to sub-grid scale heterogeneities (Taylor et al., 2011, 2012; Guillod et al.,
84 2015), the representation of soil moisture, and the possible interplay with the atmospheric
85 circulation (Boé, 2013; Hohenegger & Stevens, 2018). The complexity and the variety
86 of processes involved make the land-atmosphere interactions one of the key sources of
87 uncertainty in climate change simulations at regional scale. As an example, analyses of
88 CMIP5 models revealed considerable spread in the ability of models to reproduce ob-
89 served correlation between precipitation and soil moisture in the tropics (Williams et al.,
90 2012).

91 The various phases of the Climate Model Intercomparison Project (CMIP) give im-
92 portant milestones to measure the progress and the remaining open questions concern-
93 ing the climate modeling and in particular the parameterization of the land surface-atmosphere
94 interactions. Between phase 5 and 6 of CMIP, significant efforts have been devoted to
95 improving the atmospheric (Hourdin et al., 2020), the land surface and hydrological com-
96 ponents of the Earth System Model (ESM) of Institut Pierre Simon Laplace (IPSL) and
97 to tuning the climate model. When the fully coupled model is used, compensating er-
98 rors can hide the role played by the sub-grid scale processes that regulate a large part
99 of the exchanges of energy, water and matter between the surface and the free atmosphere
100 or constrain the related parameterizations to work in unrealistic conditions (e.g. Roehrig
101 et al., 2013; Diallo et al., 2017). On the contrary, working with individual components
102 impedes the activation of important couplings and feedbacks. Configurations with pre-
103 scribed sea surface temperature (SST) and sea ice concentration (SIC) allow us to over-
104 come these difficulties. These configurations are referred as Atmospheric Model Inter-
105 comparison Project (AMIP) configurations. Together with an intermediate configura-
106 tion, such as a nudged configuration in which the large-scale dynamics (i.e. the zonal and
107 meridional wind components) is nudged towards reanalysis (Coindreau et al., 2007; Cheruy
108 et al., 2013; Diallo et al., 2017), these AMIP-like configurations are used here to assess
109 how realistic the continental surface-atmosphere interactions simulated by the IPSL cli-
110 mate model are, and to help interpreting the fully coupled simulations produced with
111 the atmospheric (LMDZ) and land surface (ORCHIDEE) components of IPSL-Climate
112 Model (CM).

113 The focus of the present analysis is put on the processes which control the energy
114 and moisture exchange at the surface. Main features of the near surface climate over con-
115 tinentals in the historical simulations done with the full IPSL Climate Model (CM) are
116 documented in a companion paper (Boucher et al., 2020) where the biogeochemical as-
117 pects of the land surface-atmosphere coupling are considered.

118 In the first section, the major changes of LMDZ, ORCHIDEE, and their interface
119 are summarized and the simulations used for the analyses are described. The evolution
120 of the main biases in near surface variables since CMIP5 is analysed in the second sec-
121 tion and sensitivity studies are used to identify the source of these biases. The role of
122 the parameterizations and of the adjustment or tuning (Hourdin et al., 2017) is discussed.
123 In the third section the impact of the modified parameterizations on essential variables
124 of the coupling (radiation, evaporation, precipitation, superficial soil moisture) is discussed
125 for hot-spot regions (R. Koster et al., 2004) such as Central North America and and a
126 region in Sahel where the land surface coupling is strong but largely model-dependent
127 (Hohenegger et al., 2009; Boé & Terray, 2008). The third section also deals with river

128 discharge and its response to precipitation. It is a central target for a climate model for
 129 several reasons: one of them is that the freshwater discharge into the Arctic Ocean from
 130 the boreal rivers affects the global climate system by impacting the thermohaline circula-
 131 tion (Peterson et al., 2002). It is also a valuable source of information for utilization
 132 of global water resources and prevention of floods and drought which can both increase
 133 the risk for populations in the context of climate change (Arnell & Gosling, 2013; Schewe
 134 et al., 2014). For some basins it is possible to compare the results with observations which
 135 provides an assessment of the hydrological cycle over major watersheds. In the last sec-
 136 tion, the results are summarized and directions for further improvements are presented.

137 2 Model physical content and setup of the simulations

138 2.1 The atmospheric model

139 LMDZ is the atmospheric General Circulation Model (GCM) that has been devel-
 140 oped for about thirty years at the Laboratoire de Météorologie Dynamique (LMD). The
 141 versions of LMDZ used for the phase 5 and 6 (hereafter called 6A) of CMIP together with
 142 the configuration adopted are described in Hourdin et al. (2006) and Hourdin et al. (2020).
 143 The main contribution of IPSL to CMIP5 was done with a package hereafter called AP
 144 and referred to as "IPSL-CM5A" in the CMIP5 database. Version 6A is an improved
 145 version of the "new physics" package, a preliminary version of which has been tested for
 146 CMIP5 (Hourdin et al., 2020) and is referred as "IPSL-CM5B-LR" in the CMIP5 database.
 147 The changes from the AP to the "new physics" version are linked to a complete rethink-
 148 ing of the parameterizations of turbulence, convection and clouds and are described in
 149 Hourdin et al. (2013). The main model modifications between the "new physics" and
 150 6A are the revision of the eddy diffusion Yamada (1983) 1.5 order turbulent scheme al-
 151 ready implemented in the new physics, the introduction of a stochastic triggering designed
 152 to make the frequency of occurrence of new convective systems within a mesh aware of
 153 the grid cell size (Rochetin, Couvreur, et al., 2014; Rochetin, Grandpeix, et al., 2014),
 154 a modification of the thermal plume model for the representation of stratocumulus clouds
 155 (Hourdin et al., 2019), the introduction of the latent heat release associated with water
 156 freezing (not accounted for so far) and a new parameterization of non orographic grav-
 157 ity waves targeting the representation of the quasi-biennial oscillation (QBO). These changes
 158 were accompanied by a significant refinement of the vertical grid, both for the QBO is-
 159 sue and for a better representation of boundary layer clouds. The radiative codes in LMDZ
 160 are inherited from the ECMWF weather forecast model. In version AP a "large band"
 161 spectral model was used both in the thermal infrared and in the shortwave spectrum (J.-
 162 J. Morcrette, 1991). In version 6A, the infrared part was replaced by the RRTM code
 163 (Mlawer et al., 1997), based on a k-correlated scheme with 16 spectral bands. For the
 164 shortwave radiation the number of spectral intervals increased from 2 to 6 in order to
 165 better distinguish near infrared, visible and ultraviolet radiation.

166 For the setting of the 6A version, particular attention was paid to the very stable
 167 boundary layers that occur over the ice sheet plateaus, sea ice and boreal lands. Such
 168 boundary layers can experience very weak and intermittent turbulence even close to the
 169 ground surface, pushing the current state-of-the-art subgrid mixing parameterizations
 170 and underlying physical assumptions to their limits and even beyond. Together with the
 171 refinement of the vertical grid, the computation of the eddy diffusion in the Yamada (1983)
 172 scheme was revised. Minimum threshold values of the mixing length and of the stabil-
 173 ity functions of the eddy diffusion coefficient have been significantly decreased (table 2)
 174 to allow for a cut-off of turbulence at a few meters above the surface in the very stable
 175 conditions encountered over the Antarctic Plateau and to obtain more realistic sharp ver-
 176 tical gradients in very stable atmospheric boundary layers (Vignon, Hourdin, Genthon,
 177 Galle, et al., 2017). Such threshold values are often set in operational numerical mod-
 178 els to compensate for the non-representation of subgrid mixing processes and to prevent
 179 excessive near surface cooling over land in winter (e.g. Sandu et al., 2013). The sensi-

180 tivity of the continental temperature at seasonal and diurnal scale to the values of the
 181 thresholds will be discussed in sections 3.2 and 3.4. Moreover, a new numerical treat-
 182 ment of the Turbulent Kinetic Energy (TKE) equation in the new scheme (hereafter Y83-
 183 free) prevents an artificial cut-off of the turbulence at standard time step values that could
 184 occur in previous model versions even at moderate stability (Vignon, 2017; Hourdin et
 185 al., 2020).

186 The need to remove thresholds in turbulence scheme to properly model the stable
 187 Atmospheric Boundary Layer (ABL) over the Antarctic Plateau also raises the need to
 188 parameterize more explicitly the additional sources of mixing in other regions of the globe
 189 such as orography-induced small scales gravity-wave drag (Steenefeld et al., 2008) or the
 190 drag induced by vertical obstacles penetrating the boundary layers such as trees (Nepf,
 191 1999; Masson & Seity, 2009). Due to the refinement of the vertical grid of the model sev-
 192 eral layers can intersect high vegetation. The loss of large-scale kinetic energy due to these
 193 drags is converted into turbulent kinetic energy. The evaluation of the orography-induced
 194 gravity-wave drag is based on the scheme developed by (Lott, 1999), while the drag due
 195 to high vegetation is set proportional to the vegetation fraction which penetrates the bound-
 196 ary layer. The two sub-grid scale mixing processes generate TKE which is accounted for
 197 in the prognostic equation (see Appendix A for details). The impact of these new devel-
 198 opments on near-surface atmospheric variables are illustrated in section 3.4.

199 2.2 The land surface model

200 The land surface is described by the ORCHIDEE model v2.0. The ORCHIDEE
 201 model v2.0 computes primarily the fluxes of energy, water, and carbon that are exchanged
 202 between the different soil and plant reservoirs and the exchange of these fluxes with the
 203 atmosphere. In addition it computes the stocks of water and carbon in the different soil
 204 and plant reservoirs and the energy stored in the different soil and snow layers. Model
 205 state variables are prognostic, including the Leaf Area Index (LAI), as they are updated
 206 at each time step after the calculation of the fluxes between all reservoirs. The module
 207 computing dynamically the LAI, the vegetation albedo, and the soil water stress func-
 208 tion applied to transpiration is activated for all CMIP experiments, except for the Hi-
 209 gresMIP one (see section 2.4) that uses prescribed values. The vegetation properties
 210 are defined by plant functional types (PFTs) and their fraction within each grid cell is
 211 globally set from land cover maps that were derived specifically for the CMIP6 simula-
 212 tions ((Lurton et al., 2020). These maps combine the historical maps from the land use
 213 harmonization database (LUH2v2h, (Hurtt & Chini, 2011) and the maps derived from
 214 satellite observations (Bontemps et al., 2015). See ([https://orchidas.lsce.ipsl.fr/
 215 dev/lccci/](https://orchidas.lsce.ipsl.fr/dev/lccci/)) for more information. The water and energy budgets are computed at the
 216 same timestep as the atmospheric physics (Hourdin et al., 2020) using classical soil-vegetation-
 217 atmosphere transfer (SVAT) parameterizations. The most relevant modification since
 218 the version used for CMIP5 is related to the soil hydrology, the snow scheme and the back-
 219 ground albedo. The 2-layer conceptual parameterization (hereafter referred to as Choi,
 220 (Ducoudré et al., 1993)) used for CMIP5 is a double bucket model that has an upper layer
 221 with a varying depth that can appear at the surface after a rainfall event to deal with
 222 short-time processes and disappears after dry spells (Manabe, 1969). "Choi" refers to
 223 the scheme that Choissnel developed and tested for cultivated area over France. Laval
 224 (1988) showed that this model improved the sensible and latent heat flux computation
 225 on the original bucket model when introduced into the LMD Atmospheric General Cir-
 226 culation Model. In the version used for CMIP6, the vertical water transport is described
 227 using the Richard's equation (De Rosnay et al., 2002; d'Orgeval et al., 2008) discretized
 228 with 11 layers. The layer thickness increases downwards, and is doubled between each
 229 consecutive layer. The soil moisture column is active over 2 m, a free drainage condition
 230 is imposed at the bottom of the reservoir. This scheme hereafter called ctrl, as it is now
 231 the reference version for IPSL-CM, is sometimes referred to as the "11-layer" ORCHIDEE
 232 scheme. The potential of improvement of an early version of this scheme coupled with

233 the AP and "new physics" versions of LMDZ has been tested in Cheruy et al. (2013) and
 234 Campoy et al. (2013). The soil thermodynamics and in particular the soil thermal prop-
 235 erties have been revised by F. Wang et al. (2016). They have a significant impact on the
 236 surface temperature and its high frequency variability in all regions except for the moist
 237 regions (Cheruy et al., 2017). The vertical discretization for temperature is now iden-
 238 tical to that adopted for water, with a minimum soil depth increased to 10m (and even
 239 90m when the soil freezing is accounted for) so that the condition of zero flux at the bot-
 240 tom can be checked globally and annually. The soil properties (hydraulic and thermal)
 241 depend on soil moisture and soil texture, with three possible classes (sandy loam, loam,
 242 and clay loam). The dominant soil texture is assigned to each grid cell, based on the 1
 243 degree soil texture map of Zobler (1986). The soil heat capacity is parameterized as a
 244 function of the heat capacity of the dry soil and the liquid water profile and when nec-
 245 essary the ice profile. The soil freezing is allowed and diagnosed in each soil layer fol-
 246 lowing a scheme proposed by Gouttevin et al. (2012), but the latent heat release/consumption
 247 associated with water freezing/thawing is not accounted for. The freezing state of the
 248 soil mainly impacts the computation of soil thermal and hydraulic properties, reducing
 249 for instance the water infiltration capacity at soil surface. T. Wang et al. (2013) replaced
 250 the snow scheme of Chalita and Le Treut (1994) by a three-layer scheme of intermedi-
 251 ate complexity largely inspired by that proposed by Boone and Etchevers (2001). A rout-
 252 ing module (Polcher, 2003; Guimberteau, Drapeau, et al., 2012) transforms the total runoff
 253 in each sub-basin into river discharge through the ocean. This routing scheme relies on
 254 a cascade of linear reservoirs along the river network (stream reservoirs), complemented
 255 in each grid cell by two local reservoirs, to account for the delay between surface runoff
 256 and drainage, on the one hand, and overland and groundwater flow to the stream reser-
 257 voir, on the other hand. When using Choi, which does not separate total runoff into sur-
 258 face runoff and drainage, an arbitrary partitioning is imposed, with 5% feeding the fast
 259 reservoir and 95 % feeding the slow reservoir (Guimberteau et al., 2014). In the multi-
 260 layer version of ORCHIDEE, evaporation from bare soil following a supply and demand
 261 pattern that is controlled by the moisture present in the surface layers of the soil (the
 262 four soil layers of the model closest to the surface), which evaporates at the potential rate
 263 if the soil moisture supply meets the demand.

264 The continental ice-covered surfaces (ice sheets and glaciers) are not included in
 265 ORCHIDEE but they are treated in a specific module within LMDZ. Momentum and
 266 heat roughness heights as well as visible and near infrared albedos are set to constant
 267 values representative of snow conditions over the Antarctic Plateau (Vignon et al., 2018).
 268 The heat transfer in the snow and ice is parameterized as a conductive process with a
 269 fixed thermal inertia (Hourdin, 1992). The vertical grid is made of 11 vertical levels to
 270 represent the e-folding damping of thermal waves with typical periods from 1800 seconds
 271 to 240 years. The value of the snow thermal inertia was calibrated to obtain realistic sur-
 272 face temperature and diurnal cycle amplitudes in Antarctica (Vignon, Hourdin, Genthon,
 273 Gallée, et al., 2017).

274 Le Quéré et al. (2018) have recently used a version of ORCHIDEE (referred to as
 275 Orchidee-Trunk) which is similar to the version used for CMIP6 in an intercomparison
 276 project focussing on the carbon and water fluxes where 15 other land surface models (LSM)
 277 were involved. The skill scores obtained by ORCHIDEE are among the highest for most
 278 of the variables considered in this study and in particular for evapotranspiration, LAI
 279 and runoff (see table B2 in Le Quéré et al. (2018)) which are directly involved in our
 280 study.

281 **2.3 The coupling with the surface**

282 In the surface layer the boundary layer model uses Monin-Obukhov theory and bulk
 283 formulations proposed by Louis et al. (1982) to parameterize turbulent fluxes. Several
 284 modifications were made in the representation of the surface layer of LMDZ as well. First,

285 and consistently with the changes done in the boundary layer to allow strong decoupling
 286 in stable atmospheres, the so-called ‘long-tail’ stability functions from Louis et al. (1982)
 287 that artificially enhance the surface turbulent fluxes in stable conditions were replaced
 288 by more realistic ‘short-tail’ functions from King et al. (2001). This was shown to sig-
 289 nificantly improve the representation of surface temperature on the very flat ice sheet
 290 of the Antarctic plateau.

291 A second important change is related to the computation of surface roughness height
 292 z_0 . At the surface itself, heat and humidity transfer are dominated by molecular diffu-
 293 sion which is less efficient than the momentum transfer done by the pressure forces that
 294 are related to the geometry of the roughness elements of the surface (Garratt & Hicks,
 295 1973). For these reasons the roughness heights for the momentum are currently much
 296 higher than that of heat or humidity. While a unique value was used in former versions
 297 for all the model state variables, a different value is now used for horizontal momentum
 298 $z_{0,m}$ and thermodynamical variables $z_{0,h}$ or tracers $z_{0,a}$ for all individual type of sub-surface
 299 (land, sea, sea-ice, continental-ice). For each PFT ORCHIDEE used a prescribed value
 300 for the roughness height for heat and moisture independent of the development of the
 301 vegetation over continents. For a grid point composed of different types of vegetation,
 302 an effective surface roughness is calculated based on the flux conservation over the grid
 303 point. This value was also used for $z_{0,m}$ in LMDZ. Measurement campaigns often sug-
 304 gest that the roughness height for heat should be one-tenth of that for momentum for
 305 homogeneous surfaces and even less for heterogeneous surfaces (Malhi, 1996). Some stud-
 306 ies propose that over vegetated areas the roughness height can be parameterized as a func-
 307 tion of the LAI. This is the case of the model proposed by Massman (1999) and tested
 308 by Su et al. (2001) which has been implemented in ORCHIDEE v2.0. In forced mode,
 309 the dynamic roughness heights computed for each PFT as a function of the LAI help re-
 310 duce latent heat calculated in winter on temperate sites, in good agreement with multi-
 311 annual Fluxnet measurements (Figure B3, ([https://fluxnet.fluxdata.org/data/la-
 312 -thuile-dataset/](https://fluxnet.fluxdata.org/data/la-thuile-dataset/))). Still in forced mode, the dynamic roughness heights impact the
 313 river discharge at the scale of individual watersheds with significant improvements for
 314 the Danube and the Mississippi watersheds (not shown). The impact of activating the
 315 dynamical roughness height in coupled simulations is limited for the considered space
 316 and time scales (see section 3.4) but the option is activated for all CMIP6 simulations.

317 Another important change in ORCHIDEE is related to the individual albedo of the
 318 bare soil and of the 14 vegetated PFT which is now optimized with respect to MODIS
 319 observations. This calculation of the individual albedo leads to significant improvements,
 320 especially over desert and semi-arid areas where the albedo was significantly underes-
 321 timated. The improvement is illustrated by a comparison of the time series of the albedo
 322 simulated with the CMIP5 and the CMIP6 versions of the model and measured at the
 323 sites in the Sahel (Figure 1). The simulation is forced to follow the synoptic variability
 324 by relaxing the large-scale circulation toward meteorological analyses which allows di-
 325 rect comparison of the time series of the observations and the simulations (Coindreau
 326 et al., 2007; Cheruy et al., 2013).

327 The near-surface (i.e. 2 m) temperature (CMIP6 variable *tas*, which is one of the
 328 most analyzed variables in climate models especially in relation to climate change im-
 329 pacts) is diagnosed through a procedure based on the Monin-Obukhov theory (Hess &
 330 McAvaney, 1995). The procedure involves both surface and first model-level variables.
 331 In situations when turbulence is very weak and the atmospheric layer above the surface
 332 is dry but the surface soil moisture is far from the residual moisture, the procedure oc-
 333 casionally fails, leading to non-physical values for one time-step. When the procedure
 334 fails screen level temperature can reach 450K and screen level specific humidity becomes
 335 negative (see Appendix B). Since the problem occurs rarely, and when it does occur it
 336 is only during one timestep in the day (very exceptionally it can occur during two or more
 337 timesteps in the day), it was undetected in the final version used for the production of

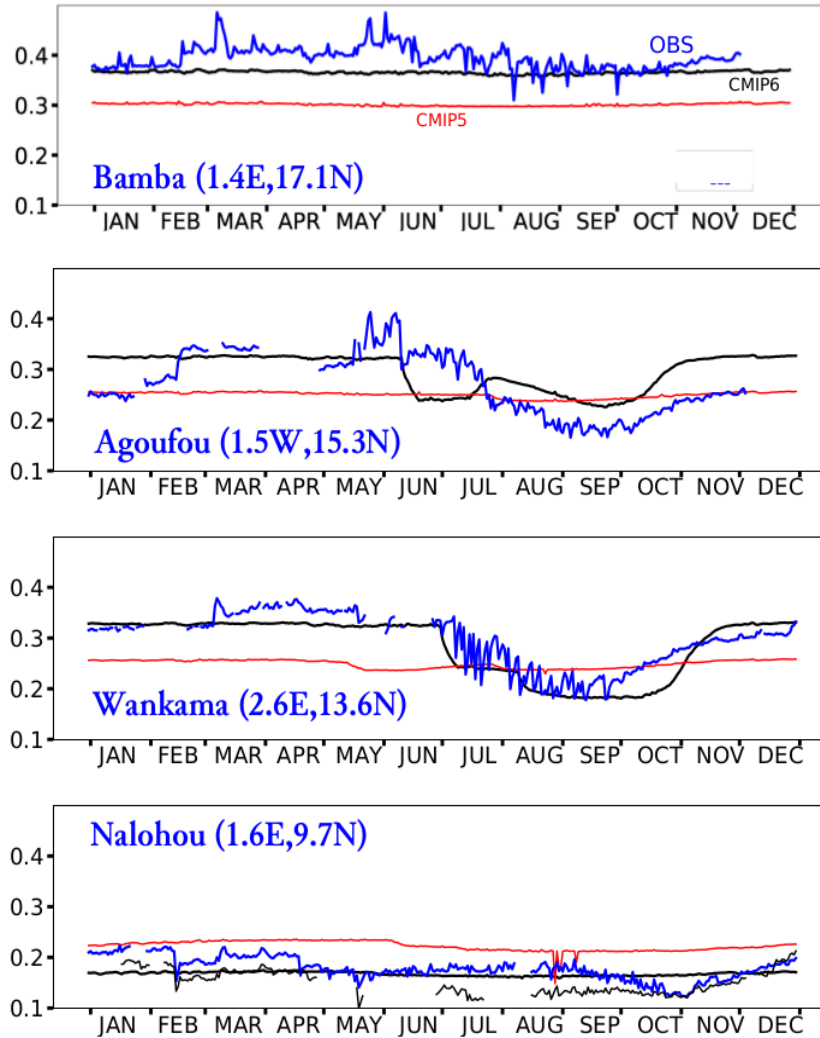


Figure 1. Time series of the surface albedo for year 2006 at Bamba, Agoufou, Wankama and Nalohou stations, from top to bottom panel respectively. Local observations (blue) are compared with nudged simulations for CMIP5 (red) and CMIP6 (black) physics. The simulation is forced to follow the synoptic variability by relaxing the large scale circulation toward meteorological analyses which allows direct comparison of the time series; Observation were obtained in 2006, the year of the AMMA Special Observing Period and are available from the AMMA-CATCH database (<http://www.amma-catch.org>)

338 the CMIP6. The problem affects the maximum daily near-surface temperature, the min-
 339 imum daily near-surface relative humidity and marginally the daily averages of these quan-
 340 tities. It occurs approximately 1700 times (respectively 2200 times) in a simulated year
 341 of the Atmospheric Model Intercomparison AMIP (respectively PreIndustrial Control
 342 (piControl, (Eyring et al., 2016))) experiments, which is very rare compared to the (365x144x142x96)
 343 times that the calculation is performed in one year of simulation. The CMIP6 experi-
 344 ments presented in this paper have not been rerun due to the time constraint imposed
 345 by the CMIP exercise, however an a posteriori correction method has been developed.
 346 All the CMIP6 data that have been affected by this problem have been either unpub-
 347 lished or corrected a posteriori and republished. The a posteriori correction method ap-
 348 plied to the published data is given in Appendix B with an estimation of the associated
 349 uncertainties which is of the order of several tenths of degrees for the daily values. Due
 350 to the low value of the reconstruction errors for the monthly mean values (30 times less
 351 than the reconstruction errors of the daily values), it was decided not to make a correc-
 352 tion to the monthly values. The great advantage is that the monthly tas values are ab-
 353 solutely consistent across all CMIP6 experiments, regardless of whether the daily val-
 354 ues have been corrected or not. According to these investigations we are confident that
 355 all the published values can be used safely for climate analysis.

356 2.4 Set-up of the simulations

357 To document the impact of the changes described in the previous sections, simu-
 358 lations forced by observed SST and SIC are produced by combining final versions of at-
 359 mospheric physics (AP and 6A) and of the soil hydrology (Choi and ctrl), namely AP-
 360 Choi (corresponding to the IPSL-CM5A in the CMIP5 database), APctrl, 6AChoi and
 361 6Actrl (corresponding to the IPSL-CM6A in the CMIP6 database) (table 1). A monthly
 362 mean climatology of SST and SIC calculated over the years 1978 to 2008 is used for the
 363 simulations in order to minimize the impact of the inter-annual variability in the eval-
 364 uation. The 6Actrl experiment is also compared with the results of the AMIP experi-
 365 ment for which a 20-member ensemble has been produced and is published in the CMIP6
 366 database. The impact of the new developments is documented thanks to an additional
 367 set of sensitivity experiments with the 6A physics where the new features of the land sur-
 368 face model and the atmospheric boundary layer are individually tested (table 2). The
 369 horizontal grid is identical to the published CMIP6-LR data (LR stands for Low Res-
 370 olution and corresponds to approx. $2.5^\circ \times 1.25^\circ$, namely 144×142 grid points (Hourdin
 371 et al., 2020)). We also document simulations performed with a much finer grid of 50 km
 372 for the HighResMIP part of the CMIP6 exercise (Haarsma et al., 2016). Comparison of
 373 these low and high resolution versions allows us to distinguish the part of the model bias
 374 linked to the coarse resolution from that more fundamentally related to the model phys-
 375 ical content. Nudged simulations in which the large-scale wind fields (zonal and merid-
 376 ional wind components) are relaxed towards the ERA-Interim reanalyzed winds (ERA-
 377 I, table 3) with a time constant of 3 hours are also used and help assess a possible con-
 378 tribution from large-scale circulation deficiencies to the continental bias. Based on pre-
 379 vious experience, it is known that a time constant of several hours (3 to 12) is short enough
 380 to constrain the largescale circulation and long enough for the physical parameteriza-
 381 tions to fully operate (for wind nudging at least). More details on this approach can be
 382 found in Diallo et al. (2017). The first three years of all experiments, corresponding to
 383 the spin-up time of the hydrological model, are disregarded in the analysis.

384 2.5 Reference datasets

385 The sets of global gridded data used as a reference to evaluate the sensitivity exper-
 386 iments are listed in table 3. They consist of a site-observations upscaled products for
 387 evaporation (Jung et al., 2011), satellite-based land evaporation and root-zone soil mois-
 388 ture derived through data assimilation processes in the Global Land Evaporation Am-

Table 1. Reference simulations: APChoi corresponds to the IPSL-CM5A configuration used for CMIP5 and 6Actrl corresponds to the IPSL-CM6A configuration used for CMIP6. The boundary conditions used (climatology (clim) or actual values of SST and Sea-Ice (actual)) are indicated in the second column.

Experiment	boundary conditions	Atmosphere	Vertical levels	Land-surface	duration
APChoi	clim	AP	39	Choi	20 years
APctrl	clim	AP	39	ctrl	20 years
6AChoi	clim	6A	79	Choi	20 years
6Actrl	clim	6A	79	ctrl	20 years
AMIP	actual	6A	79	ctrl	1978-1998

Table 2. Sensitivity experiments for processes impacting the interactions between the land surface and the atmosphere. The reference atmospheric physics is 6A with 79 vertical levels and the reference LSM is ctrl. The last four lines of the table refer to the sensitivity experiments to the sub-grid scale orography (SSO) schemes, the reference values for 6A are $gk_{lift} = 0.1$ and $gk_{drag} = 0.6$, gk_{lift} (respectively gk_{drag}) correspond to C_d (respectively C_l) in Lott (1999)

AMIP-Experiment	Description
NoOro	Deactivating orography induced small scale gravity wave drag
NoTree	Deactivating vertical obstacle penetrating boundary layer drag
NoSnowFreez	Deactivating soil freezing and replacing the snow scheme of Chalita and Le Treut (1994) by T. Wang et al. (2013)
Noz0Su	Deactivating dynamical roughness heights (Su et al., 2001) and using prescribed values with $z_{0_m} = z_{0_h}$
6Arsol	Activating resistance to bare soil evaporation
6Aric	No increased mixing in the stable PBL: ric=0.20 (reference=0.18) and lmximin=0
6Aric83lmx	Artificially increased mixing in the stable PBL: ric=0.143, lmximin=1 (reference=0)
6A-L+	Increased lift effect (SSO): $gk_{lift} = 1.0$
6A-L-	Decreased lift effect (SSO): $gk_{lift} = 0.0$
6A-D+	Increased block flow drag amplitude by (SSO): $gk_{drag} = 1.2$
6A-D-	Decreased block flow drag amplitude by (SSO): $gk_{drag} = 0.2$

389 sterdam Model (GLEAM) (Martens et al., 2017) and the ESA-CCI blended active and
390 passive microwave retrieval of surface soil moisture (Dorigo et al., 2017), CERES-EBAF
391 for surface shortwave radiation (Kato et al., 2013) and the Global Precipitation Clima-
392 tology Project (GPCP) monthly product resulting from an integration of various satel-
393 lite data sets and a gauge measurements analysis over land (Adler et al., 2003) for the
394 precipitation. The total column integrated water vapor is evaluated using the reanaly-
395 sis and extension of the NASA Water Vapor Project (NVAP) data set which comprises
396 a combination of radiosonde observations, Television and Infrared Operational Satellite
397 (TIROS) Operational Vertical Sounders (TOVS), and Special Sensor Microwave/Imager
398 (SSM/I) data sets (Vonder Haar et al., 2012). The river discharges are extracted from
399 the Global Runoff Data Center (GRDC) database (Milliman & Farnsworth, 2011). The
400 Snow Cover Extent (SCE) is extracted from the output from the Interactive Multisen-
401 sor Snow and Ice Mapping System (IMS) at the National Ice Center (NIC) processed

402 at Rutgers University and included in the NOAA Climate Data Record (CDR) of North-
 403 ern Hemisphere (NH) Snow Cover Extent. For the minimum and maximum daily tem-
 404 perature, we used the Climatic Research Unit (CRU) Time-Series (TS) version 4.01 of
 405 high-resolution gridded data (Harris et al., 2014).

406 The observations cover a period of at least 10 years compatible with the SST and
 407 SIC climatology used to force the model. We suggest that not considering the exact same
 408 periods for the simulations and the observations only has a minor impact on the results
 409 given that the model internal variability is damped due to the use of a climatological SST.

Table 3. Global gridded data sets used as reference

Variable (monthly means)	Dataset	Date	Reference
Radiation	CERES-EBAF-L3B-Ed2-8	2001-2012	(Kato et al., 2013)
Precipitation	GPCP long-term-mean	1979-2005	(Adler et al., 2003)
Evapotranspiration	In Situ upscaled products (over land)	1982-2011	(Jung & Coauthors, 2011)
Evapotranspiration	GLEAM	2001-2011	(Martens et al., 2017)
Surface soil moisture	ESA-CCI	2001-2011	(Dorigo et al., 2017)
Surface soil moisture	GLEAM	2001-2011	(Martens et al., 2017)
Air temperature (min/max daily)	CRU	2001-2010	(Harris et al., 2014)
Air temperature	ERA-Interim	1979-2014	(Dee et al., 2011)
Horizontal winds	ERA-Interim	1979-2014	(Dee et al., 2011)
Total Precipitable Water	NVAP-M	1988-2009	(Vonder Haar et al., 2012)
River Discharge	GRDC	1981-2010	(Milliman & Farnsworth, 2011)
Snow Cover	NOAA-CDR-SCE	2000-2009	(Robinson et al., 2012)

410 In the supplementary material, ERA-5 data ([https://cds.climate.copernicus](https://cds.climate.copernicus.eu/cdsapp#!/home)
 411 [.eu/cdsapp#!/home](https://cds.climate.copernicus.eu/cdsapp#!/home)) are used as a benchmark in addition to ERA-Interim data to eval-
 412 uate the bias in the air-temperature (Figure S1).

413 3 Surface energy budget and temperature

414 3.1 Impact of the revision of the eddy diffusion parameterization

415 The improvements resulting from the revision of the turbulent scheme between the
 416 AP version and the 6A version of LMDZ are illustrated on Figure 2, showing the mean
 417 seasonal cycle of the air temperature for the first 3 atmospheric level of LMDZ (version
 418 AP and 6A) together with the measurements recorded at 6 levels on the 45m height mast
 419 at Dome C (75.1S, 123.3E), Antarctic Plateau. For version AP (Figure 2,a) an overall
 420 winter-time warm bias (up to 10K) in the surface layer is noteworthy. This version was
 421 also unable to properly reproduce the dynamical behavior of the very stable Antarctic
 422 boundary layers (Vignon et al., 2018) and further analysis of the vertical temperature
 423 profile in the first few hundred meters above Dome C revealed a significant underesti-
 424 mation of the climatological temperature inversion (not shown). For version 6A, both
 425 the near-surface temperature and its vertical gradient are in good agreement with ob-
 426 servations from the surface up to the top of the mast (Figure 2). The dynamics of very
 427 stable boundary layers is also much better simulated (Vignon et al., 2018) than in ver-

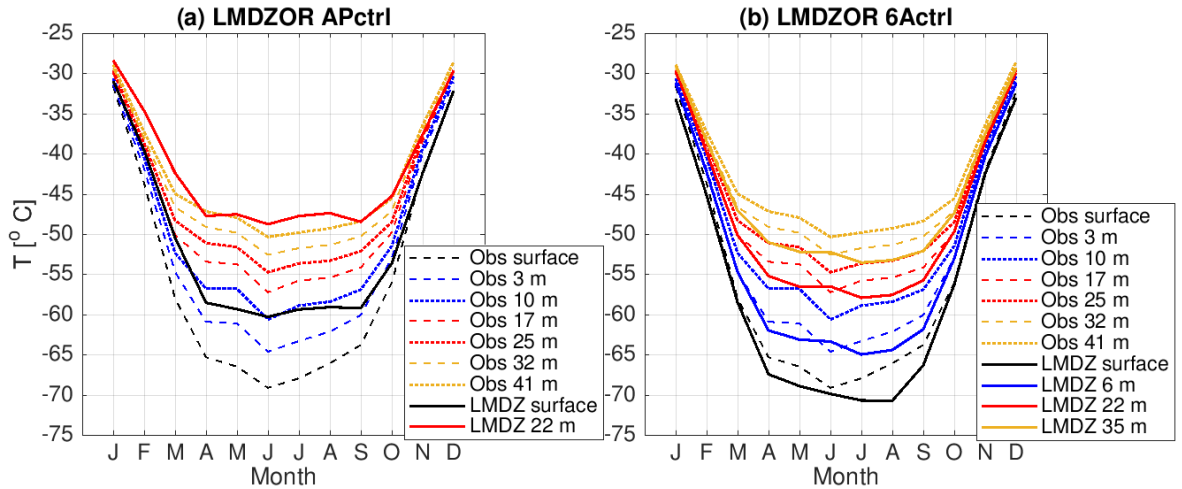


Figure 2. Time series of the near-surface monthly mean temperature at Dome C (75.1S, 123.3E), Antarctic Plateau. Solid lines show the APctrl simulation (a) and the 6Actrl simulation (b). Dashed and dotted lines refer to the 2011-2018 observational dataset along a 45-m meteorological mast (Genthon et al., 2013).

428 sion AP. Figure 3 shows how version AP and 6A perform in a single-column configura-
 429 tion used to simulate the test case of DIurnal land-atmosphere Coupling Experiment (DICE)
 430 (Kansas, latitude 37.65N, longitude 263.265E) far from the ice sheets regions. The simu-
 431 lations cover a period of three days and three nights and the last night which is stable
 432 and cloudfree is well suited to test the boundary layer scheme under stable condi-
 433 tion. The hydrological scheme is bypassed by prescribing the ratio β of evaporation to
 434 potential evaporation and the surface thermal inertia to a value adjusted to the DICE
 435 case during the full run (Ait-Mesbah et al., 2015). For night-time the near surface tem-
 436 perature inversion is much stronger than for the AP run (Figure 3 a). The sensible heat
 437 flux is reduced with the 6A version and closer to the observations than the AP version
 438 (Figure 3 b), which produced a too strong vertical mixing.

439 **3.2 Relative impact of atmospheric and land surface components on the** 440 **biases of near-surface variables**

441 Most of the biases in evaporation, 2m-temperature, shortwave downward radiation
 442 at the surface, surface albedo, precipitation and total precipitable water can be analyzed
 443 by inspecting zonal mean variables over the continents (Figure 4). To further comment
 444 regional aspects, maps of mean annual, JJA and DJF bias in 2m-temperature are de-
 445 picted in Figure 5. The corresponding bias maps are displayed in the supplementary in-
 446 formation for the shortwave downward radiation at the surface (Figure B3), evaporation
 447 (Figure B3), surface albedo (Figure B3), precipitation (Figure B3) and total precipitable
 448 water (Figure B3). The maps corresponding to the first member of the AMIP ensem-
 449 ble are also plotted, in order to confirm the representativity of the 6Actrl experiment with
 450 respect to the AMIP published data. We verified that the feature discussed hereafter are
 451 shared by the other members of the AMIP ensemble. The statistical significance of the
 452 changes caused by the new land surface and atmospheric physics is assessed geographi-
 453 cally for each studied variable in Figures 6 (6Actrl-6AChoi) and B3 (6Actrl-APctrl), with
 454 very similar results to the differences maps for APctrl-APChoi and 6AChoi-APChoi (not
 455 shown).

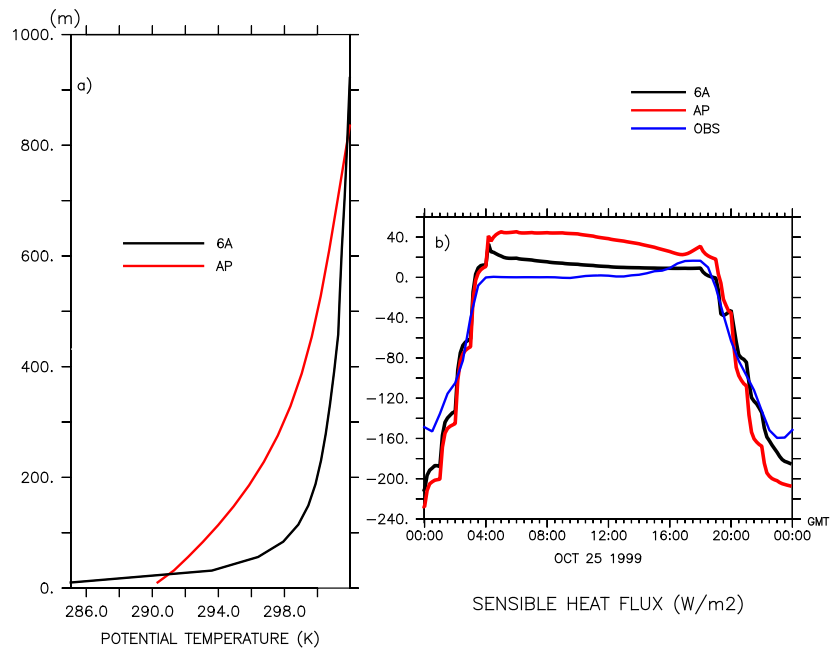


Figure 3. Temperature profile (a) and sensible heat flux (b) for the third night (stable) of the DICE case simulated with the AP (red) and 6A (black) version of the atmospheric physics. The observed sensible heat flux is plotted together with the simulations (blue).

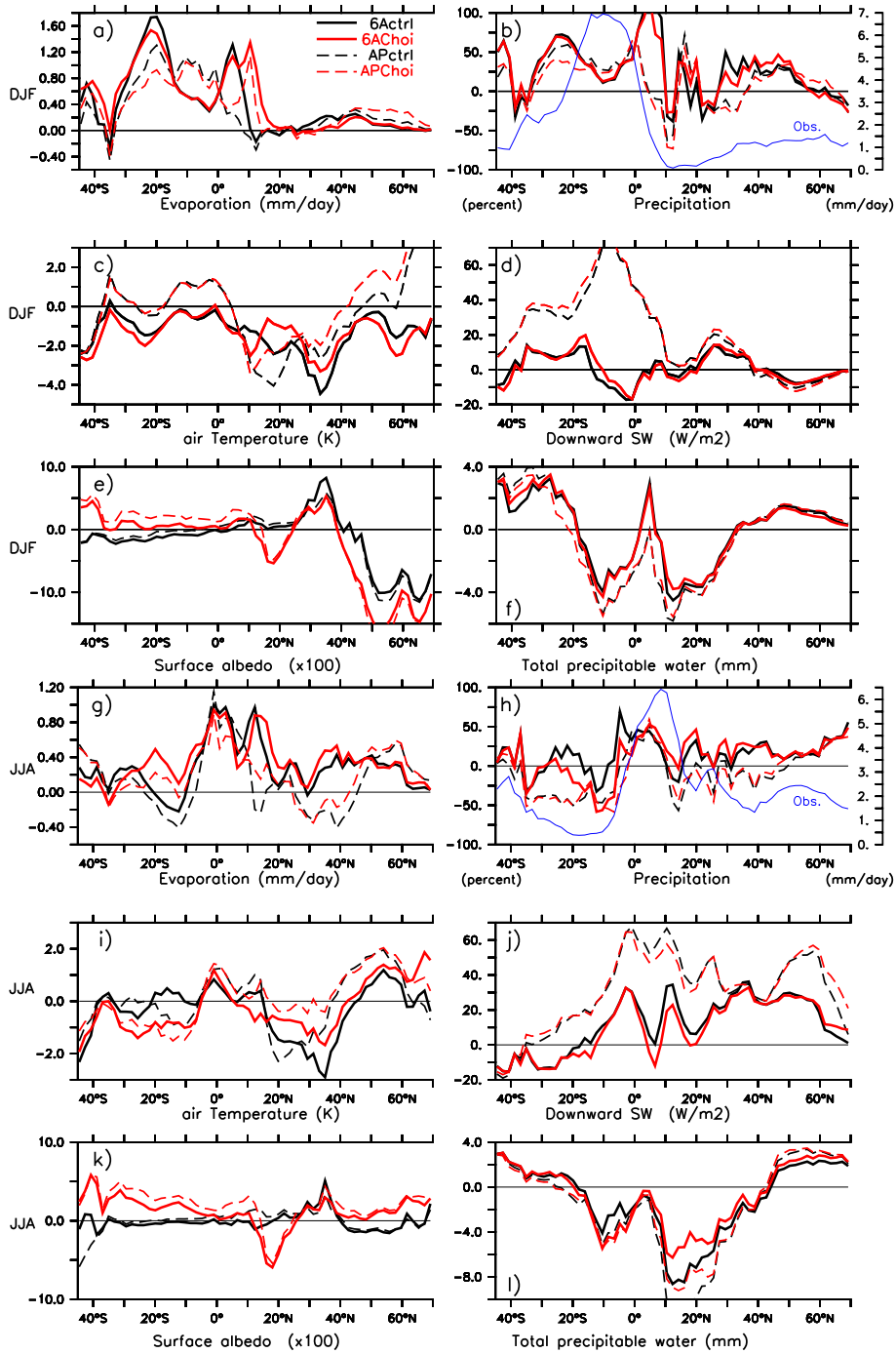


Figure 4. Zonal mean bias in December-January-February (DJF) and June-July-August (JJA) over continents for the evaporation (a,g), the precipitation (b,h), the air temperature (c,i), the downward shortwave (SW) radiation (d,j), the surface albedo (e,k), the total precipitable water (f,l) in 6Actrl (thick black curve), 6AChoi (dashed black curve), APctrl (thick red curve) and APChoi (dashed red curve). For precipitation the blue curve corresponds to the absolute value of the observations (yaxis on the right side). The references are described in table 3

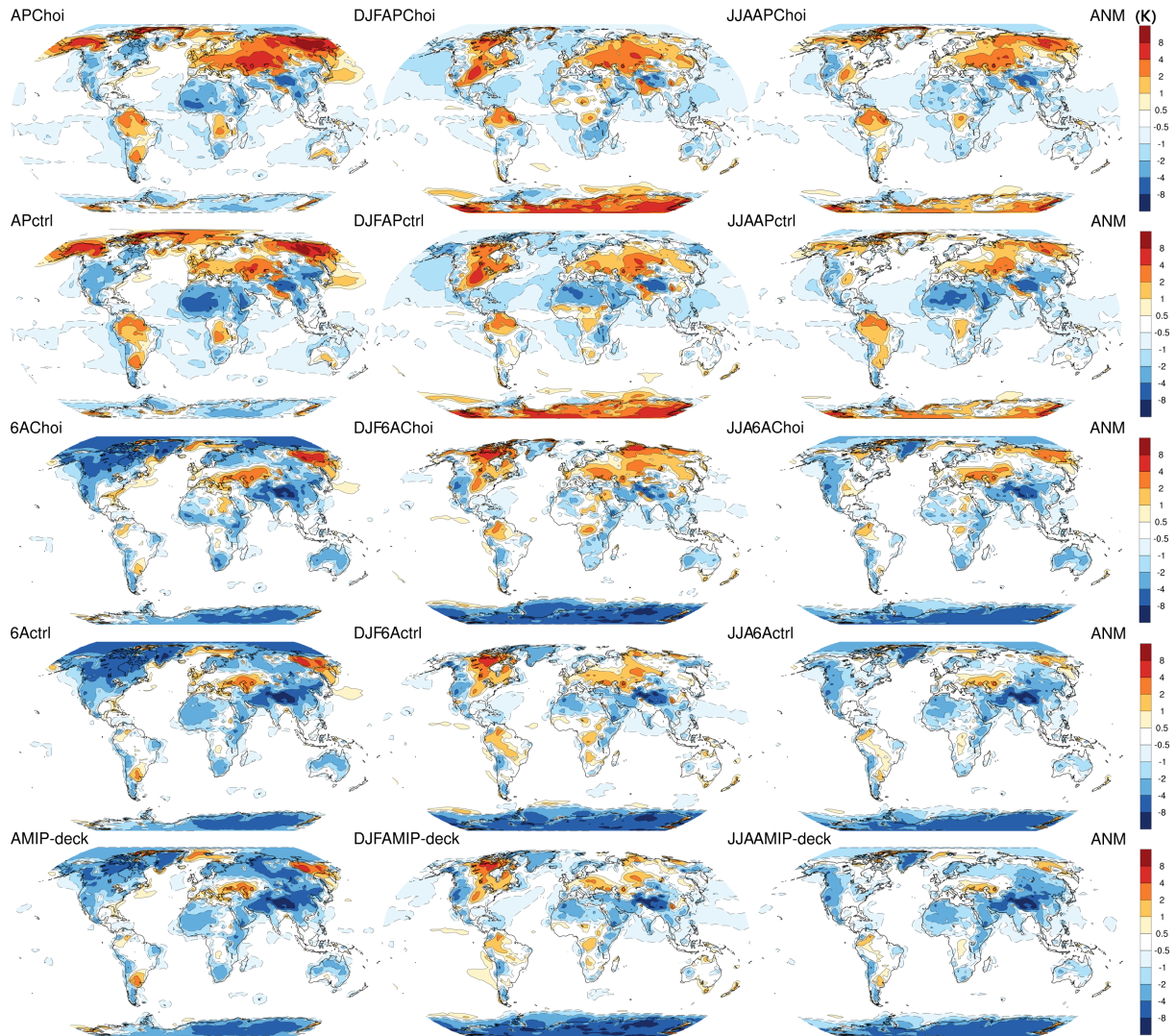


Figure 5. Mean multi-annual bias in 2m temperature (tas) for December-January-February (first column) and for June-July-August (middle column) and for the full year (last column) in the APChoi (first row), APctrl (second row), 6AChoi (third row), 6Actrl (fourth row) and AMIP configurations (fifth row). The reference is given by ERAI reanalysis averaged for the 1979-2014 period

456 A clear improvement of the CMIP6 reference configuration 6Actrl is related to the
 457 radiation budget. This improvement is illustrated by the reduction of the bias in the down-
 458 ward shortwave (SW) radiation at the surface in 6Actrl (Figure 4 d and j) and can be
 459 attributed to the improvement of the representation of the Cloud Radiative Effect (CRE)
 460 coming from the modification in the parameterizations and to the improved tuning of
 461 the model free parameters targeting the CRE (Hourdin et al., 2020). Consistently with
 462 the overall reduction in the SW radiation bias (Figure B3) and in the evaporation bias
 463 especially over the continental United States (Figure B3) the strong warm bias over the
 464 mid-latitudes in summer (Figure 5) that was shared by many models participating in
 465 CMIP5 (Cheruy et al., 2014) is reduced in the 6Actrl configuration used for CMIP6. Over
 466 the continental United States, Al-Yaari et al. (2019) also showed that the general agree-
 467 ment between areas of strong warm bias and areas of strong precipitation and soil mois-
 468 ture deficits is good. In the 6Actrl configuration the precipitation deficit is also signif-
 469 icantly reduced (Figure B3) and the surface soil moisture is in better agreement with the
 470 observations (see section 4.1). In connection with the developments on the vertical dif-
 471 fusion scheme, the warm bias that extended over a large part of the polar and boreal re-
 472 gions in winter is reduced or even replaced by a cold bias over part of the Arctic con-
 473 tinent and Ocean, Greenland and Antarctica (Figure 5). The cold bias is probably over-
 474 estimated over Greenland, the Arctic Ocean and Antarctica due to a warm bias diagnosed
 475 in ERA-I (Jakobson et al., 2012; Reeves Eyre & Zeng, 2017; Vignon et al., 2018). When
 476 using ERA-5, as reference dataset instead of ERA-I, the bias over Greenland is reduced
 477 in DJF (not shown). Over the Arctic continent Lindsay et al. (2014) report that ERA-I
 478 has a bias of less than 0.5K compared to the observations.

479 As a result of the new snow scheme and of the optimization with respect to the MODIS
 480 observations, the surface albedo in the ctrl model is improved in most regions in win-
 481 ter (Figure 4 e, B3) and over deserts (notably the Sahara) over the year. The new snow
 482 scheme improves the snow cover which was significantly underestimated with Choi (Fig-
 483 ure 7). With the exception of the surface albedo and to a lesser extent the evaporation,
 484 the overall structure of the bias is only marginally sensitive to the land surface scheme
 485 whose impact is mostly relevant at the regional scale (Figures 5, 6, B3, B3, B3, B3, B3).

486 When considering the continents globally, Choi and ctrl both overestimate the evap-
 487 oration (especially in winter) regardless of the atmospheric model with which it is cou-
 488 pled. This overestimation is slightly less for ctrl (Table 4), albeit this result is modulated
 489 at regional scale (Figure 6). Investigating the minimum and maximum daily tempera-
 490 ture shows a widespread warm bias of daily minimum temperature over the mid-latitude
 491 (Figure 8). This bias is present over the whole year for the AP physical package used
 492 for CMIP5 and only in JJA for the 6A package used for CMIP6, it is very marginally
 493 sensitive to the land surface scheme. This is consistent with the reduction of the turbu-
 494 lent mixing in the PBL for the stable boundary layers obtained with the 6A atmospheric
 495 physics and with the results of Wei et al. (2017) which suggested that a bias in the sim-
 496 ulated PBL mixing could very likely contribute to the temperature bias common to most
 497 of the models that participated to CMIP5 with AMIP experiments. The moist atmo-
 498 spheric bias over the mid-latitudes in JJA (Figure 4 l) could contribute to the warm bias
 499 of daily minimum temperature by minimizing the nocturnal radiative cooling but fur-
 500 ther investigation is needed to explain this bias which is shared by other models partic-
 501 ipating in CMIP6.

502 3.3 Atmospheric process sensitivity to the LSM choice

503 The above analysis has shown that, for most variables and skills considered, the
 504 changes due to the atmospheric physics are larger and more broadly significant than the
 505 ones due to the land surface physics, as confirmed by the comparison between Figures
 506 B3 and 6, respectively. We detail here the sensitivity of the 6A atmospheric physics to
 507 the LSM choice (Figure 6). The differences between 6Achoi and 6Actrl are statistically

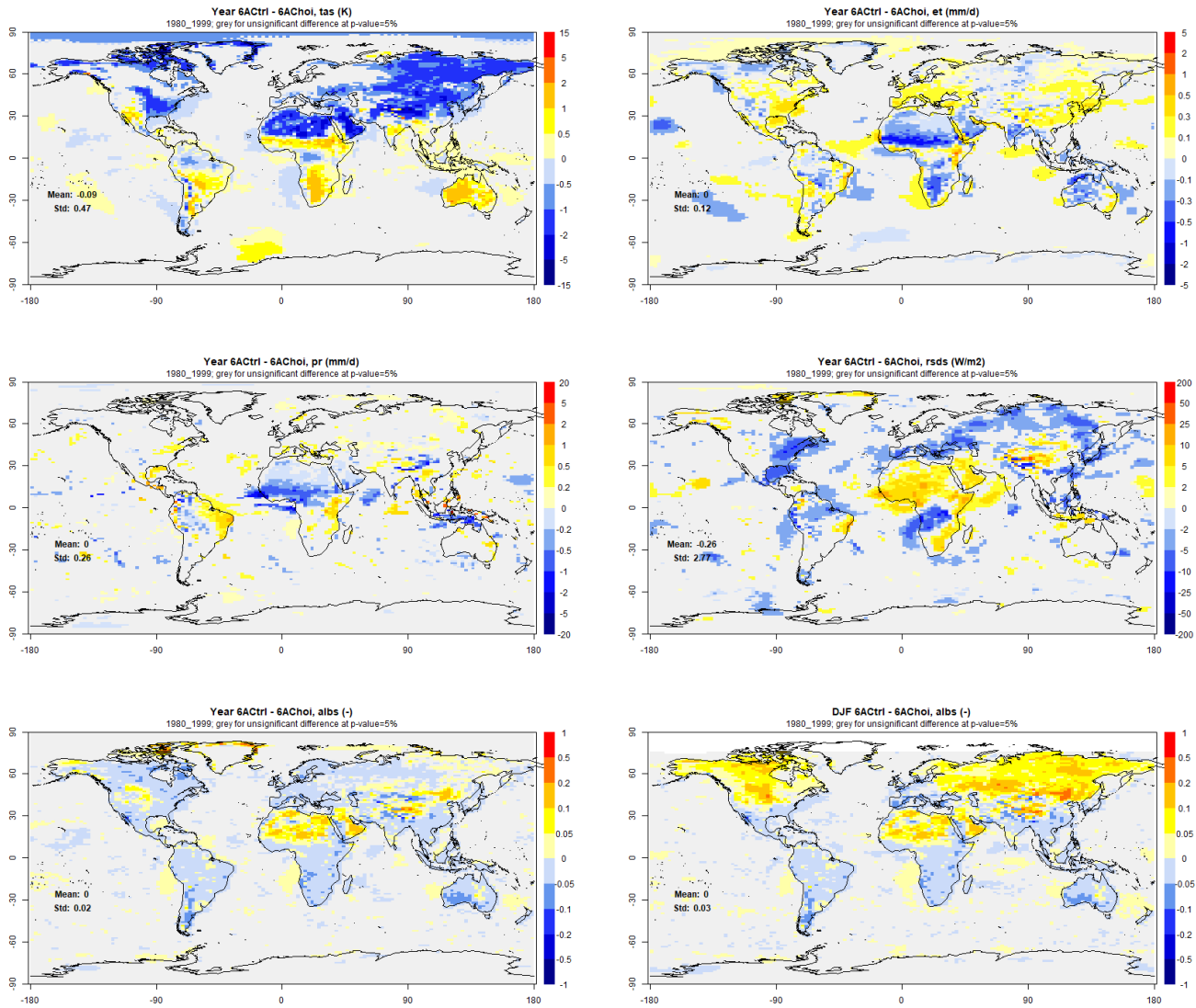


Figure 6. Significance of the multi-annual differences between configurations 6Actrl and 6Achoi, with grey coloring where the difference is not statistically significant based on Student's t-test (with a p-value < 0.05). The first five maps show the yearly mean differences for the air temperature, evaporation, precipitation, downward SW radiation at the surface, surface albedo, and the bottom right map shows the winter (DJF) difference in surface albedo. The displayed means and standard deviations are calculated over the whole globe including non significant points.

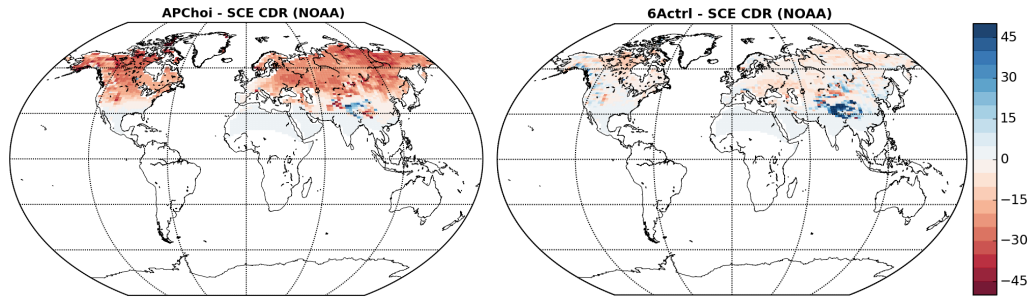


Figure 7. Mean annual bias in the snow fraction for the APChoi (left) and 6Actrl (right) configurations. The reference is taken from the NOAA Climate Data Record (CDR) Snow Cover Extent (SCE) diagnosed from the Interactive Multisensor Snow and Ice Mapping System (IMS) at the National Ice Center (NIC)

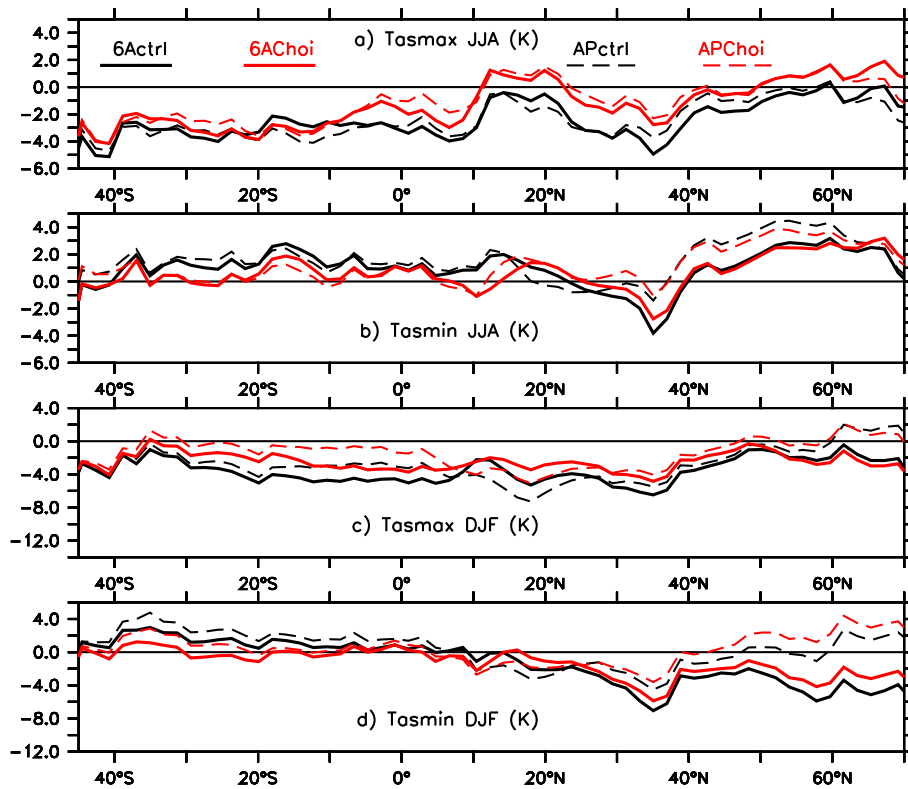


Figure 8. zonal mean bias over continents in the seasonal means of minimum and maximum daily temperature for the reference configurations (thick black curve: 6Actrl, dashed black curve: 6Achoi, thick red curve: APctrl, dashed red curve: APchoi)

508 significant (at the 5% level) over most of the continents for all variables but precipita-
 509 tion. The seasonal differences (not show but for winter surface albedo) are very consis-
 510 tent with the yearly differences. Ctrl induces a significant cooling over an extended re-
 511 gion going from Siberia to China (up to 3K locally in absolute value). This cooling is
 512 accompanied with an increase in evapotranspiration, some local reductions of the down-
 513 ward SW radiation, but also a widespread decrease of surface albedo (mostly driven by
 514 the summer season thus by vegetation), which is probably overruled by the large decrease
 515 of albedo in winter. In contrast, large land areas of the southern hemisphere exhibit a
 516 significant warming from Choi to ctrl, along with an evaporation decrease, a decrease
 517 of surface albedo, and a downward SW radiation increase. Two exceptions can be iso-
 518 lated to the cooling/warming response to evaporation increase/decrease. The first one
 519 is the Sahara, where air temperature is reduced with ctrl, despite significant reduction
 520 of evaporation and increase of incoming SW radiation: the reason is the substantial albedo
 521 increase in this area, like in most sparsely vegetated zones. The second exception com-
 522 prises the humid equatorial areas (inter-tropical convergence zone), where surface air tem-
 523 perature decreases without any significant evaporation change: there, the main driver
 524 seems to be the reduction of incoming surface radiation, likely related to precipitation
 525 increases, although these changes are rarely significant, and mostly in JJA. Precipita-
 526 tion is also significantly impacted by the choice of the LSM over monsoon regions, like
 527 Western Africa in JJA and Southern Amazonia in DJF, where ctrl tends to reduce evap-
 528 oration and precipitation. The few spots over tropical oceans where the change in pre-
 529 cipitation and evaporation are significant over the tropics are probably due to slight mod-
 530 ifications of the circulation in response for instance to the temperature changes. How-
 531 ever, the amplitude of the changes is very low with respect to the typical oceanic val-
 532 ues in those regions. When considering the continents globally, Choi and ctrl both over-
 533 estimate the evaporation (especially in winter). This overestimation is slightly less for
 534 ctrl (Table 4), albeit this result is modulated at regional scale (Figure B3).

Table 4. Mean continental biases in DJF and JJA for 2m-temperature, evaporation, surface downward radiation, albedo and for the reference simulations (APChoi, APctrl, 6AChoi, 6Actrl). APChoi corresponds to the IPSL-CM5A configuration used for CMIP5 and 6Actrl corresponds to the IPSL-CM6A configuration used for CMIP6. The last line corresponds to the mean value over continents calculated with the observation described in table 3.

Experiment	2m-T (K)	Evaporation (mm/day)	Precipitation (mm/day)	sfc SW (down) (W/m ²)	albedo (x100)
DJF					
APChoi	0.19	0.33	0.41	16.4	-0.83
APctrl	-0.39	0.30	0.47	15.2	-0.72
6AChoi	-1.40	0.36	0.57	1.07	-0.33
6Actrl	-1.47	0.34	0.58	0.63	-0.29
Obs	279.4	0.99	1.82	155.4	17.2
JJA					
APChoi	0.31	0.18	0.03	36.5	1.73
APctrl	0.05	0.11	0.03	35.8	0.19
6AChoi	-0.15	0.36	0.42	14.2	0.89
6Actrl	-0.37	0.28	0.37	16.27	0.01
Obs	293.8	1.75	2.06	227.5	18.

535

3.4 Sensitivity experiments

536

537

In order to further interpret the above results we use the sensitivity experiments described in table 2 of section 2.4.

538

539

540

541

542

543

544

545

546

547

548

549

550

551

Sensitivity simulations to the strength of the decoupling in stable condition were performed by changing the values of the minimal mixing length (l_{mixmin}), and of the critical Richardson number (ric) above which the stability functions of the turbulent diffusion coefficient reach their lower-bound value (see Fig. 2 in Vignon, van de Wiel, et al. (2017) for details). Those two thresholds enhance the mixing and prevent the turbulence cut-off in very stable conditions (Tab. 2, 6Aric, 6Aric83lmix). Figure 9 shows the impact of the sensitivity experiments on the zonal means in JJA and DJF. North of 60N, the near surface temperature is highly sensitive to these thresholds. Allowing less decoupling (Tab. 2, 6Ari83lmix) significantly reduces the cold bias over continental areas in winter but it deteriorates the vertical temperature gradient over the Antarctic Plateau shown in Figure 2. A further increase of the decoupling with respect to the configuration adopted for CMIP6 (Tab. 2, 6Aric) leads to a reduction of the winter-time minimal temperature but does not impact the night-time bias in summer for the 6A version (not shown).

552

553

554

555

556

As expected, the orography-induced TKE production (Tab. 2, NoOro, also see Appendix A) tends to warm the mid- and boreal- latitudes in winter which partially counterbalances the effect of the reduced vertical diffusion for the stable boundary layers (not shown). The impact of deactivating the drag induced by the vegetation penetrating the boundary layer (Tab.2, NoTree) is negligible for the near-surface temperature (not shown).

557

558

559

560

561

562

563

564

565

566

567

568

569

A sensitivity simulation focusing on the evaporation for the ctrl model was also designed to target the bare soil evaporation which can reach the potential rate when the moisture in the first four layers of the soil is higher than the residual moisture (Tab.2, 6Arsol). It is likely that the potential rate of evaporation leads to an overestimation of evaporation when patches of soil begin to dry out in the grid cell. To overcome this defect a resistance to bare soil evaporation can be added to the aerodynamic resistance. This approach has been implemented in ORCHIDEE using the formulation proposed by Sellers et al. (1986). The activation of this option reduces the evaporation (Figure 9-a and g). However, amplifying the SW radiation bias at the surface over the mid-latitude north (Figure 9- d and j) and reducing the evaporative cooling results in a strong warm bias (Figure 9-c and i). The impact of the deactivating the dynamical roughness height (Tab.2, noz0Su) is detected at the regional scale on the evaporation and the temperature but it is quite limited for the considered space and time scales (not shown).

570

3.5 Specific regional changes

571

Several biases mostly rely on regional features and are discussed in this section.

572

573

574

575

576

577

578

579

580

581

582

583

584

- Sahara
The cold bias between 15N and 30N in all simulations and for all seasons (Figures 4-c and -i) is mostly the signature of a cold bias over the Sahara (Figure 5). It may be due to aerosol specification or to the failure to consider emissivity lower than the unit in the radiative transfer calculations. The cold bias is less pronounced with the AP physics because the strong positive bias in the downwelling SW radiation and the under-estimation of the surface albedo compensate the excessive surface cooling due to the overestimated value of the surface emissivity.
- Tibetan Plateau and High-mountain Asia
There is an overall cold bias in winter between 30N and 40N (Figure 4 i, 5) which is particularly strong over the Tibetan plateau and high-Mountain Asia where it is associated with a surface albedo bias (Figure B3) and an over-estimation of the snow fraction (Figure 7). The albedo bias is not present in ORCHIDEE stand-

585 alone simulations (not shown), and is lower when the old snow scheme is activated.
 586 This is consistent with a difficulty of the land-atmosphere model to melt snow lead-
 587 ing to a too high albedo inducing a positive feedback on the temperature because
 588 of a deficit in net SW radiation at the surface. The weaker bias produced by the
 589 old snow scheme is consistent with the underestimation of the snow albedo which
 590 was already documented by T. Wang et al. (2013). These results confirm that land
 591 surface atmosphere feedbacks play a significant role in this region. The temper-
 592 ature and the albedo biases are weaker in the HighRes simulations (not shown)
 593 and in nudged simulations (Figure B3). The weakening of the bias obtained with
 594 the increase in resolution or with the wind nudging confirms that the regional cir-
 595 culation is an important component of the High-mountain Asia climate. A high
 596 resolution allows us to represent more realistic contrasts of the snow cover between
 597 the lowlands and the high mountains. It is also a way to better simulate the role
 598 of the orographic barrier played by the High-mountain Asia that stops the north-
 599 ward transport of moisture originating from the Indian subcontinent. This bar-
 600 rier explains the dryness of the Tibetan plateau (Sabin et al., 2013; Ménégoz et
 601 al., 2014; Krishnan et al., 2019) where an excess of moisture flux is simulated at
 602 coarse resolution, inducing a positive bias of snow cover that is enhanced by sur-
 603 face feedback. In the same way, by correcting the regional circulation, the nudg-
 604 ing can reduce the positive bias of snow cover which impacts the surface albedo.

- 605 • Central Asian lowlands

606 The more realistic representation of the snow albedo and the increased decoupling
 607 for stable boundary layers help obtain more realistic near-surface temperatures
 608 but does not eliminate the strong warm bias present in winter on the Central Asian
 609 lowlands in CMIP5 (Figure 5, DJF). The temperature bias is further reduced when
 610 the large-scale circulation is relaxed toward meteorological analysis. The nudg-
 611 ing reduces also the total precipitable water (not shown) that is greatly overes-
 612 timated in this region. These results suggest that the large-scale dynamics con-
 613 tributes to the bias by a too strong moisture advection, the latter limiting radi-
 614 ative cooling. A residual negative bias in surface albedo (Figure B3 DJF) can also
 615 contribute to the warm bias. In summer, the warm bias is also present but it is
 616 mainly associated with an excess of SW radiation at the surface.

- 617 • Eastern Siberia

618 Regardless of the model version, a strong warm bias persists in the extreme north-
 619 east of Siberia, north of the Sea of Okhotsk and north of the Bering Sea. The bias
 620 is not present in the nudged-by-wind simulations (Figure B3) and it is less marked
 621 when the new snow scheme and the soil freezing are activated (NoSnowFreez ex-
 622 periment in table 2, not shown). The bias is also reduced when the decoupling is
 623 increased. This suggests that both large-scale circulation and local processes and
 624 their interactions play a significant role in this region.

- 625 • Southern Great Plains

626 While substantial biases are reduced with respect to the APChoi configuration of
 627 the model used for CMIP5, a warm bias remains over the Southern Great Plains.
 628 The Clouds Above the United States and Errors at the Surface (CAUSES) exper-
 629 iment (C. J. Morcrette et al., 2018) in which IPSL participated highlighted a strong
 630 deficit of deep-cloud events (reduced in the CMIP6 version with respect to the ver-
 631 sion that participated in the intercomparison ; Kwinten Van Weverberg, personal
 632 communication). Concerning the precipitation, Van Weverberg et al. (2018, their
 633 Fig. 13) show that none of the models that participated in CAUSES are able to
 634 correctly represent the diurnal cycle of the precipitation evaluated with the At-
 635 mospheric Radiation Measurement Best Estimate (Xie et al., 2010). The nudg-
 636 ing does not allow to reduce the bias. In this region, rainfall comes from two dif-
 637 ferent convective regimes. The first regime is associated with a local triggering of
 638 convection induced by daytime heating, the second regime corresponds to the prop-
 639 agating systems over the Great Plains, initiated in the lee of the Rockies (Klein

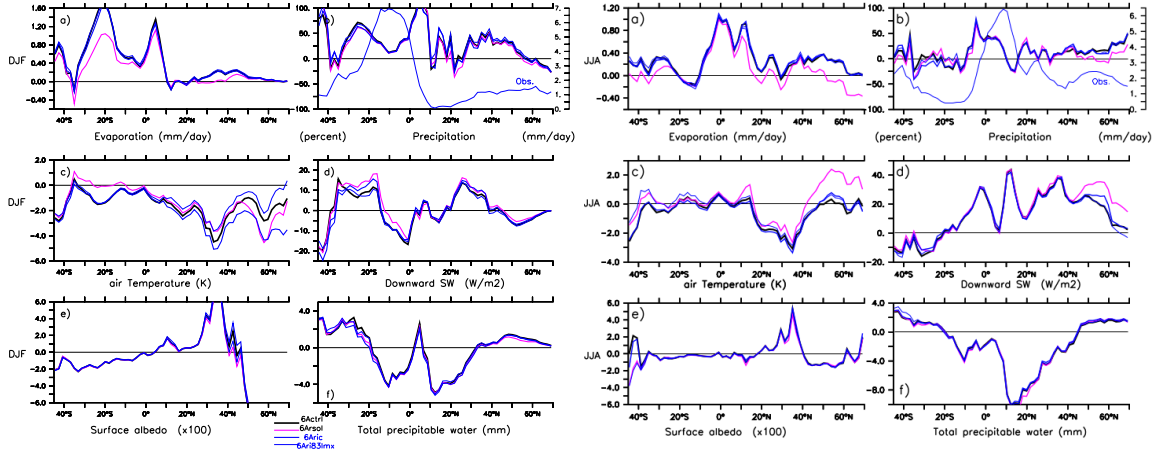


Figure 9. Zonal mean bias in DJF and JJA over the continents for the evaporation (a, g), the precipitation in percent and the absolute value of the observation (b, h), the air temperature (c, i), the downward SW radiation at the surface (d,j), the surface albedo (k,e), the total precipitable water (f,l) in the reference experiment 6Actrl (thick black curve), in sensitivity experiments for the turbulent mixing 6Aric (thick blue curve), in 6Aric83lms (blue thin curve) and in sensitivity experiment with a resistance to bare soil evaporation activated (thick pink curve)

640 et al., 2006). The precipitation associated with the first regime is fairly well rep-
 641 resented by the LMDZ model with a maximum delayed in the afternoon which is
 642 a robust improvement of the convective scheme (Rio et al., 2009; Hourdin et al.,
 643 2020). The night-time maximum due to propagative systems is absent in most mod-
 644 els of CMIP5/CMIP6 and in particular in the simulations of LMDZ, which has
 645 no parameterization for this type of propagative system.

646 • Amazonia and Central Africa

647 The strong warm bias present in the simulation with the AP atmospheric physics
 648 does not exist in the simulation with the 6A physics (Figure 5) as a result of the
 649 strong reduction of the downward SW radiation at the surface discussed in sec-
 650 tion 3.2.

651 **3.6 Tuning of the global model and near surface temperature over land**

652 Significant efforts have been made to improve the physical content of the param-
 653 eterizations. Yet, they remain an idealized and approximate representation of processes.
 654 As a consequence adjustment and tuning are unavoidable when all the atmospheric, land
 655 surface and oceanic components are coupled (Hourdin et al., 2017).

656 A tuning of sub-grid scale orography (SSO) was performed to better represent the
 657 atmospheric heat transport toward the Arctic Ocean which is a key region for sea-ice for-
 658 mation and melting. The SSO schemes are applied to represent the blocking effect of oro-
 659 graphy at low levels, and the breaking of gravity waves (see Lott (1998) and more details
 660 in the Appendix A). The sensitivity experiments (Tab. 2) reveal that the SSO tuning
 661 has an impact on the near surface temperature mostly during the cold season, from Novem-
 662 ber to March (see Fig. 10), which is consistent with the established impacts of oro-
 663 graphy onto the large scale atmospheric circulation (Holton, 2004). Increasing the block-
 664 ing effect of orography through the drag scheme cools Eurasia, and warms western North
 665 America. This is consistent with a large blocking effect over the Rockies when increas-
 666 ing the drag, inducing anomalous southerly warm advection upstream, and northerly cold
 667 advection downstream (Holton, 2004). The sensitivity to the lift that modifies the flow

668 direction shows different effects, with warm anomalies upstream of the Rockies and Hi-
 669 malayas and cold anomalies downstream of the Rockies and Himalayas, but with a larger
 670 amplitude, different location and with a zonal-wavenumber 2 structure. The lift effect
 671 results from applying a force perpendicular to the local flow over orographic barriers. It
 672 causes larger meridional flow anomalies than the drag, which explains the stronger im-
 673 pact in terms of surface air temperature. The tuning of the version 6A was mainly done
 674 by increasing the drag, and slightly reducing the lift parameter so that the tuning may
 675 have contributed to enhance the cold bias over Siberia, while reducing it over North Amer-
 676 ica. However, the temperature anomalies explained by the new tuning remain small when
 677 compared to the bias itself.

678 An essential aspect of the tuning is to ensure that the radiative budget at the top
 679 of the atmosphere is in equilibrium and that the latitudinal distribution of each com-
 680 ponents of the radiative budget is as close as possible to the observations. A particular
 681 care was given to the tuning of free model parameters impacting the top of the atmo-
 682 sphere (TOA) radiation budget (Hourdin et al., 2017). Interestingly, none of the sensi-
 683 tivity studies described above strongly impacted the TOA radiative budget. This indi-
 684 cates that specific tuning targeting the land surface processes can be done independently
 685 to some extent. Such an approach has not been adopted for the 6A version of the IPSL-
 686 CM but it could improve the performances of the model and reduce some bias in future
 687 versions of the model (Li et al., 2019).

688 **4 Improvement of the realism of the hydrological cycle in the coupled** 689 **continental surface-atmosphere system**

690 The impact of the more physical hydrological scheme (ctrl) used for CMIP6 (sec-
 691 tion 2.2) and the impact of the more realistic convective precipitation documented in Hourdin
 692 et al. (2020) on the hydrological cycle is addressed in this section in two specific ways:
 693 the analysis of moisture and energy coupling at the surface at regional spatial-scale and
 694 monthly time-scale and the analysis of the seasonal cycle of precipitation and river dis-
 695 charge at the scale of individual watersheds.

696 **4.1 Soil moisture-evaporation-radiation-precipitation coupling**

697 The impact of the modified parameterizations on surface soil moisture, net SW ra-
 698 diation at the surface, evaporation and precipitation is documented at regional scale in
 699 order to insure homogeneous climate conditions to prevail. We focus on two hot-spot re-
 700 gions (R. Koster et al., 2004) where the soil moisture-atmosphere coupling is strong: the
 701 Central North America (CNA) region as defined in the Special Report on Managing the
 702 Risks of Extreme Events and Disasters to Advance Climate Change Adaptation (SREX)
 703 (S. Seneviratne et al., 2012) and a box in Sahel (-10,30E,0N-20N). A third region cor-
 704 responding to Western Europe (WE) where the coupling is weaker is also considered. The
 705 grid points corresponding to the WE box are selected according to the *KoeppeGeiger*
 706 climate classification system (Kottek et al., 2006) (region 21 in Figure B3).

707 For these regions, combined distributions of soil surface moisture, evaporation, net
 708 radiation at the surface and precipitation for the four reference configurations (6Actrl,
 709 APctrl, APChoi, 6AChoi) and for different sets of observations (Tab 3) are constructed
 710 based on monthly values for a 10-year long period in which all observations are avail-
 711 able (2001-2010).

712 First considering the distribution for the simulated surface soil moisture itself, the
 713 regional histograms of the surface soil moisture show that the Choi land surface hydro-
 714 logical scheme produces a very narrow distribution with unrealistic null value of the sur-
 715 face soil moisture for lower boundary and low maximum values of the surface soil mois-
 716 ture (not shown). This characteristics of the surface soil moisture with the Choi scheme

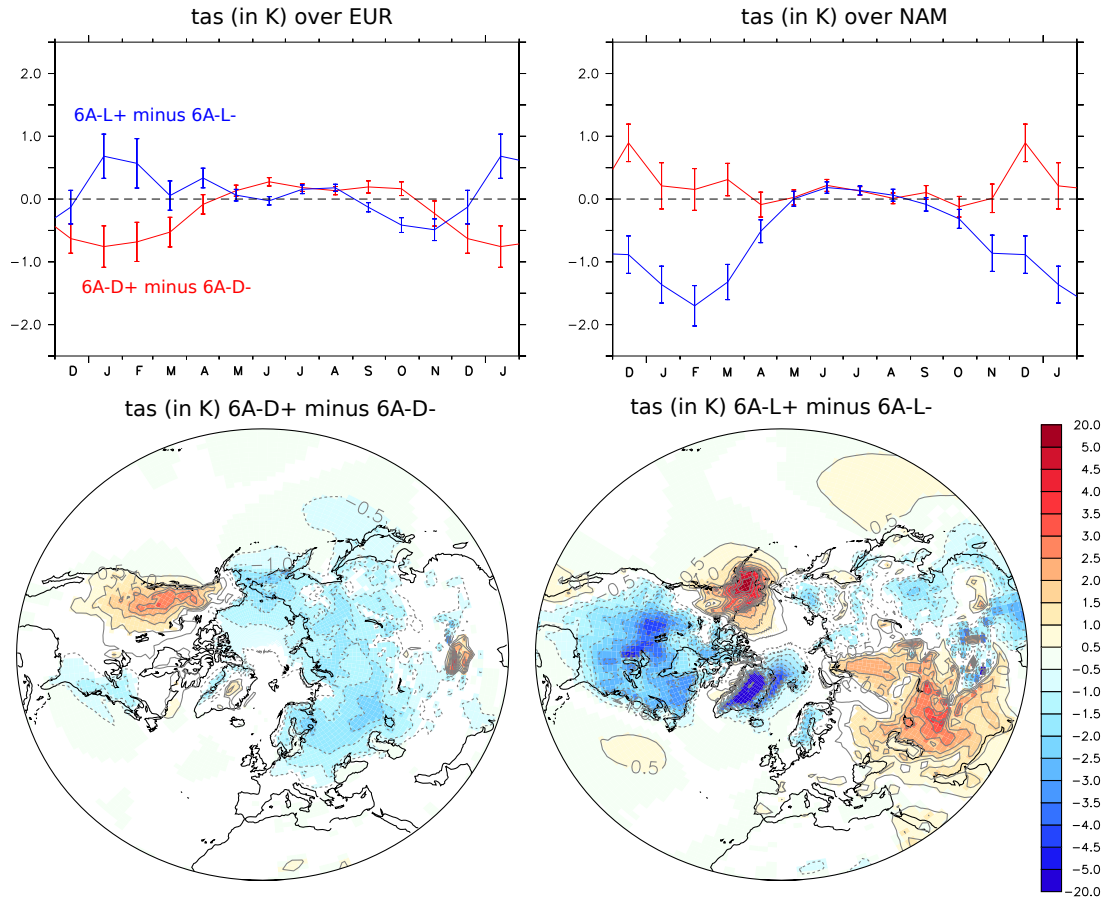


Figure 10. Top panel: 2m-temperature (CMIP6 variable tas) anomalies (in K) induced by the drag and lift parameters over (left) Eurasia (EUR, 20N-80N, 10W-180E) and (right) North America (NAM, 20N-80N, 180W-10W). The blue line indicates the difference between 6A-L+ and 6A-L-. The red line indicates the difference between 6A-D+ and 6A-D-. Bottom panels: surface air temperature anomalies (in K) induced by the (left) drag and (right) lift parameters in the Northern Hemisphere. Colors are shown only for significant areas (p-value of Student t-test lower than 10%).

717 can be explained by the crude representation of the hydrology by this scheme for which
718 the surface layer exists only intermittently. When considering the GLEAM and ESA-
719 CCI soil moisture products, the width of the distribution is significantly smaller with the
720 ESA-CCI product than with the GLEAM product (not shown). The fact that GLEAM
721 takes the upper 0–10cm into account while ESA-CCI correlates better with soil mois-
722 ture up to 5cm depth (Dorigo et al., 2017) while the superficial soil moisture in the sim-
723 ulations corresponds to the moisture in the top 10cm of soil might contribute to the dif-
724 ferences. In addition, GLEAM and ESA-CCI soil moisture products are considered as
725 observations but they are highly dependent on the underlying models used to produce
726 them and therefore suffer limits identified by R. D. Koster et al. (2009) that call for great
727 caution regarding the reliability of the absolute values retrieved. For these reasons we
728 prefer using the standardized soil moisture index defined in R. D. Koster et al. (2009,
729 see their Eq. 1) and the soil-moisture information at monthly time scale is mostly used
730 to discriminate between very dry, moderately dry, moderately moist and very moist soils
731 in the corresponding regional distributions for evaporation, net SW radiation at the sur-
732 face and precipitation.

733 For soil moisture in the Sahel region (Fig. 11) the summer observations feature a
734 U-shaped distribution in which dry and saturated states prevail. This U-shaped distri-
735 bution is reproduced by both schemes (Choi and ctrl) with strong differences: Choi fav-
736 ors the moistest contents much more than the observations while ctrl leads to a tri-modal
737 distribution. This feature has been observed for several other regions with different cli-
738 mate and is the signature of using one dominant soil texture among three possible ones
739 in each grid cell of the region, while in reality, many different soil textures coexist and
740 lead to a mixed behavior. However, the U-shape is also present indicating that the scheme
741 tends to favor dry or saturated situations for each texture as well. For all regions, the
742 highest value of the net SW radiation is overestimated by as much as $20 W.m^{-2}$. This
743 holds for both AP and 6A versions of the model and for each soil moisture quartile. Var-
744 ious hypothesis can be formulated: this bias can either rely on a difficulty in processing
745 CERES observations to retrieve the net radiation at the surface or rely on LMDZ. In this
746 case, a problem with the radiative transfer code or a lack of simulated clouds or an un-
747 derestimation of their radiative impact can be invoked. For the Sahel, when the surface
748 is moist, the 6Actrl configuration tends to underestimate the occurrence of situations
749 with an elevated evaporation rate and overestimate the occurrence of situations with low-
750 values of the net SW radiation (second and third column in figure 11). This feature can
751 be interpreted as a too frequent occurrence of radiation-limited evaporative regimes with
752 respect to the soil moisture-limited evaporative regimes in this region. For CNA and for
753 AP physics radiation is either insensitive to soil moisture (APChoi) or the low radiation
754 is surprisingly associated with the driest soil quartile (APctrl) while, for 6A physics, low
755 radiation associated with extended cloud cover is rather associated with the wettest quar-
756 tile, which is consistent with the CERES product. Over both SGP and Sahel and for the
757 driest surface soil moisture quartile, AP tends to favor little or no rainfall at the monthly
758 time scale, probably over-simulating dry events. This feature is much weaker with 6A
759 physics, and in better agreement with the observations (bottom row in Figures 11 and
760 12). When Choi hydrology is activated with 6A physics, dry soils tend to have a sustained
761 rate of evaporation, while the 11-layer hydrology also allows low evaporation rates con-
762 sistent with the observations. When AP physics is activated, dry soils tend to be asso-
763 ciated with too weak evaporation rates, this feature being more pronounced with 11-layer
764 hydrology. Additional information concerning the evolution of the performances of the
765 atmospheric model over Sahel with the AP and 6A atmospheric physics are given in Diallo
766 et al. (2017). In the hot-spot regions, the 6Actrl configuration used for CMIP6 is the clos-
767 est to observations due to both improved atmospheric physics and representation of soil
768 hydrology. Low precipitation rates (at monthly time-scale) associated with dry soil are
769 also over-estimated in Western Europe. In this region where the soil moisture-atmosphere
770 coupling is expected not to be dominant, the simulated net SW radiation, the simulated

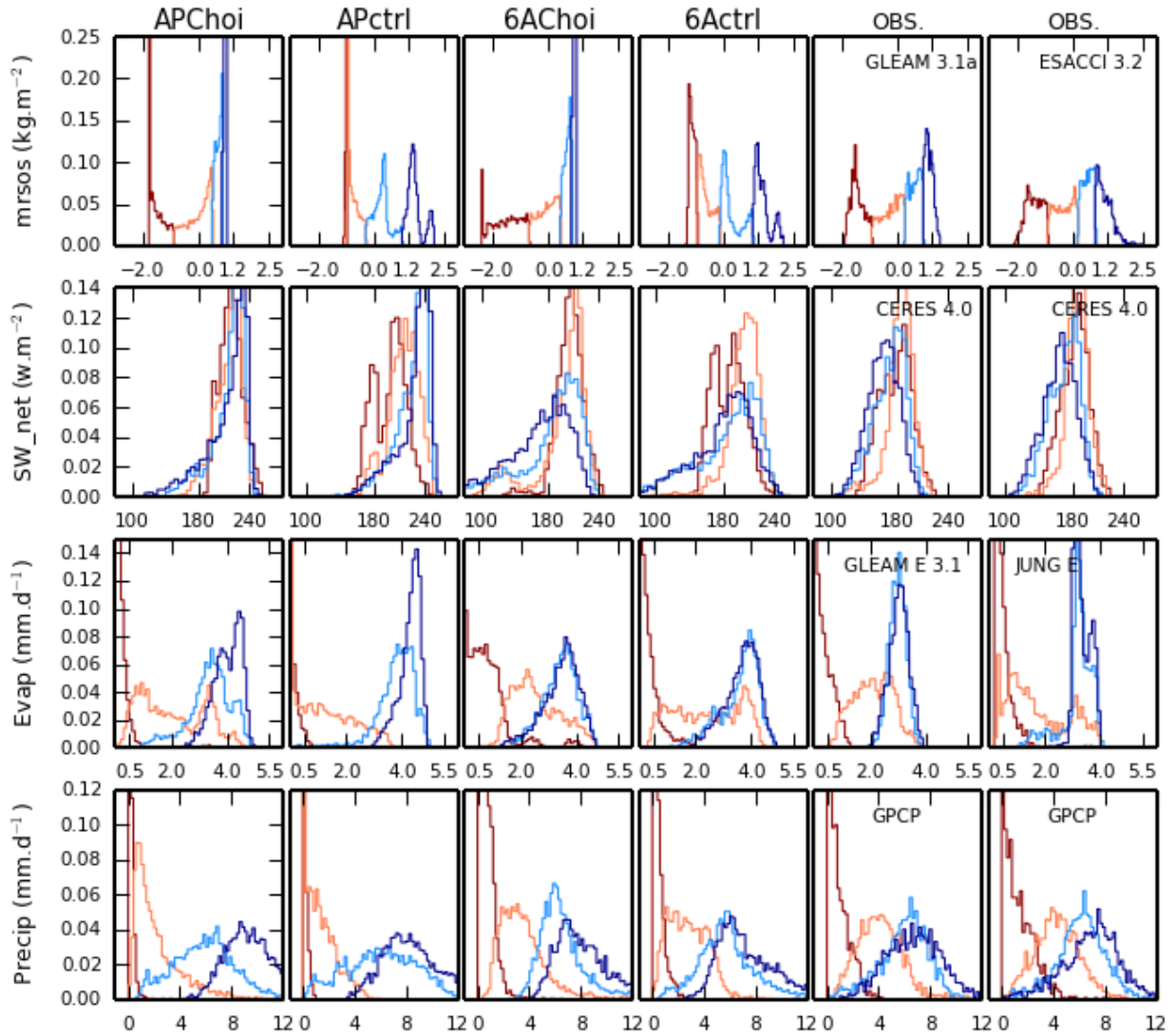


Figure 11. Regional histograms computed from monthly values of the individual grid points corresponding to the Sahel box (-10:30E,0:20N) in JJA. The histograms are constructed for a 10-year long period in which all observations are available (2001-2010). Each row is dedicated to a particular variable: surface standardized soil moisture (first row), net SW radiation at the surface (second row), evaporation (third row), and precipitation (fourth row). The first four columns correspond to the reference experiments, the last two columns correspond to the different sets of observations indicated above the corresponding histograms. The colors depict the PDF from the minimum to first quartile (dark red) from first quartile to the median (pale orange), from median to third quartile (cyan line) and from the third quartile to the maximum (blue line). For soil moisture, the y-axis is cut at .25 (representing 25% of the quartile) for the sake of readability but the driest quartile peaks at 0.8 (corresponding to 80% of the quartile) for APctrl and the moister quartile peaks at .8 for APChoi and APctrl. For evaporation the y-axis is cut at .14 (corresponding to 14% of a quartile) but 55% (APChoi) and 90% (APctrl) of the evaporation associated with the first quartile is less than 0.1 mm/d. For the precipitation, the y-axis is cut at .12 but 70% , 85%, 15 % , 40 % of the precipitation associated with the driest soil moisture quartile are less than 0.1 mm/d for APChoi, APctrl, 6AChoi and 6Actrl and 20%, 10 % for GLEAM and ESA-CCI.

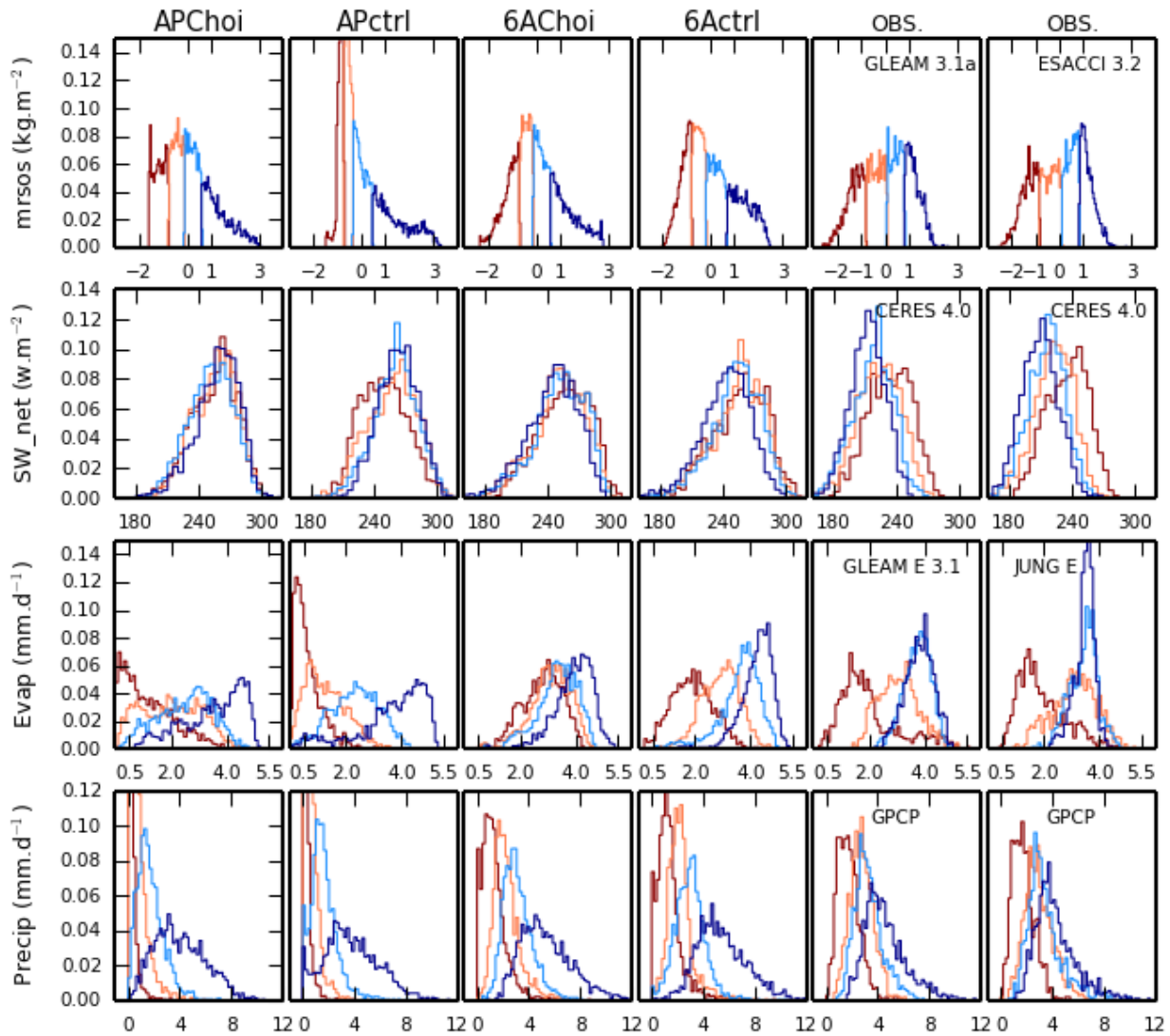


Figure 12. Regional histograms computed from monthly values of the individual grid points corresponding to the SREX CNA region (S. Seneviratne et al., 2012) in JJA. The histograms are constructed for a 10-year long period in which all observations are available (2001-2010). Each row is dedicated to a particular variable: surface standardized soil moisture (mrsos, first row), net SW radiation at the surface (second row), evaporation (third row) and precipitation (fourth row). The first four columns correspond to the four reference experiments and the last two column to the different sets of observations indicated above the corresponding histograms. The colors depict the PDF from the minimum to first quartile (dark red) from first quartile to the median (pale orange), from median to third quartile (cyan line) and from the third quartile to the maximum (blue line).

771 evaporation and the simulated precipitation appear to be more sensitive to the soil mois-
 772 ture than the observed ones (Figure B3).

773 4.2 Seasonal cycle of precipitation and river discharge

774 Figure 13 shows the seasonal cycle of precipitation observed and simulated by the
 775 four sensitivity experiments described above for 14 major watersheds together with the
 776 seasonal cycle of the river discharge observed and simulated at 14 stations on the rivers
 777 of the same major basins. For 4 out of the 5 boreal basins (Yukon, McKenzie, Yenisei,
 778 Lena) the precipitation is often overestimated in all configurations. For some basins in-
 779 cluding Mississippi, Congo and Amazonia, the seasonal cycle of simulated precipitation
 780 is significantly improved in volume or in phase in the configuration used for CMIP6 (6Ac-
 781 ctrl). For instance, in Tocantins basin in the Cerrado, the duration of the dry season is
 782 now reduced in agreement with the observations. This improvement can be attributed
 783 to changes in the parameterizations of the atmospheric physics. The impact of the land
 784 surface model is limited, except over some mid-latitude basins such as the Danube where
 785 the volume of precipitation is controlled by atmospheric physics and continental hydrolog-
 786 ical processes, and is overestimated with the 6Actrl configuration used for CMIP6. With the 6Ac-
 787 ctrl configuration, simulated river discharges are also improved for the Mississippi, Ama-
 788 zonia, Congo, owing to improved precipitation volume. The seasonal timing of river flow
 789 is different from that of rainfall because of the time needed for water to circulate in soils
 790 and along river systems after it has reached the ground. This timing is usually correct,
 791 with errors resulting from those of the simulated precipitation (e.g. intensity and loca-
 792 tion of rainfall events inside the watersheds), simulated land surface processes (e.g. snowmelt
 793 dynamics, permafrost, transit times in the soil), and the fact that residence times of the
 794 routing reservoirs only depend on the type of reservoir (stream, overland, groundwater)
 795 and the grid cell slope, while other regional factors can be important. In particular, the
 796 absence of floodplains in all the simulations largely explains the overestimation of river
 797 discharge in the Niger (d’Orgeval et al., 2008) and Congo, and may contribute to the early
 798 peak flows of the Amazon (Guimberteau, Drapeau, et al., 2012). The parameterizations
 799 of the land surface processes have a major effect in the five Arctic rivers, with a higher
 800 flow and earlier maximum when ground freezing is activated. This effect improves the
 801 simulated discharge in the two basins with the largest fraction of permafrost (Yenisei and
 802 Lena, in eastern Siberia). In the other three basins (Ob, Yukon, McKenzie), the extent
 803 of frozen soils may be overestimated, and the overestimation of the river discharge by
 804 6Actrl can also be related to the lack of dams and floodplains in the model (Gouttevin
 805 et al., 2012), with a potential feedback on permafrost extent, since a stronger cooling is
 806 required to freeze a wet soil than a dry soil. The Brahmaputra (India) discharge shows
 807 improved volume and seasonality with the 6Actrl configuration, while the maximum of
 808 the precipitation is underestimated. For this particular river that originates from the Angsi
 809 glacier located in Tibet, the change in atmospheric physics improves the timing while
 810 the maximum discharge is improved (reduced) with the activation of the soil freezing.
 811 This non-intuitive impact of soil freezing is caused by an atmospheric feedback, with less
 812 precipitation in the watershed if the freezing is activated. Yet, the positive bias of all sim-
 813 ulated discharges might rather be related to massive irrigation in this basin (Guimberteau,
 814 Laval, et al., 2012), which is not taken into account in these simulations.

815 5 Concluding discussion

816 The quality of the coupled atmosphere-land continental surface system implemented
 817 in the IPSL-CM for CMIP6 is evaluated and the relative role of atmospheric and land
 818 surface processes in controlling the coupling at the surface is analyzed and quantified.
 819 The following conclusions are reached:

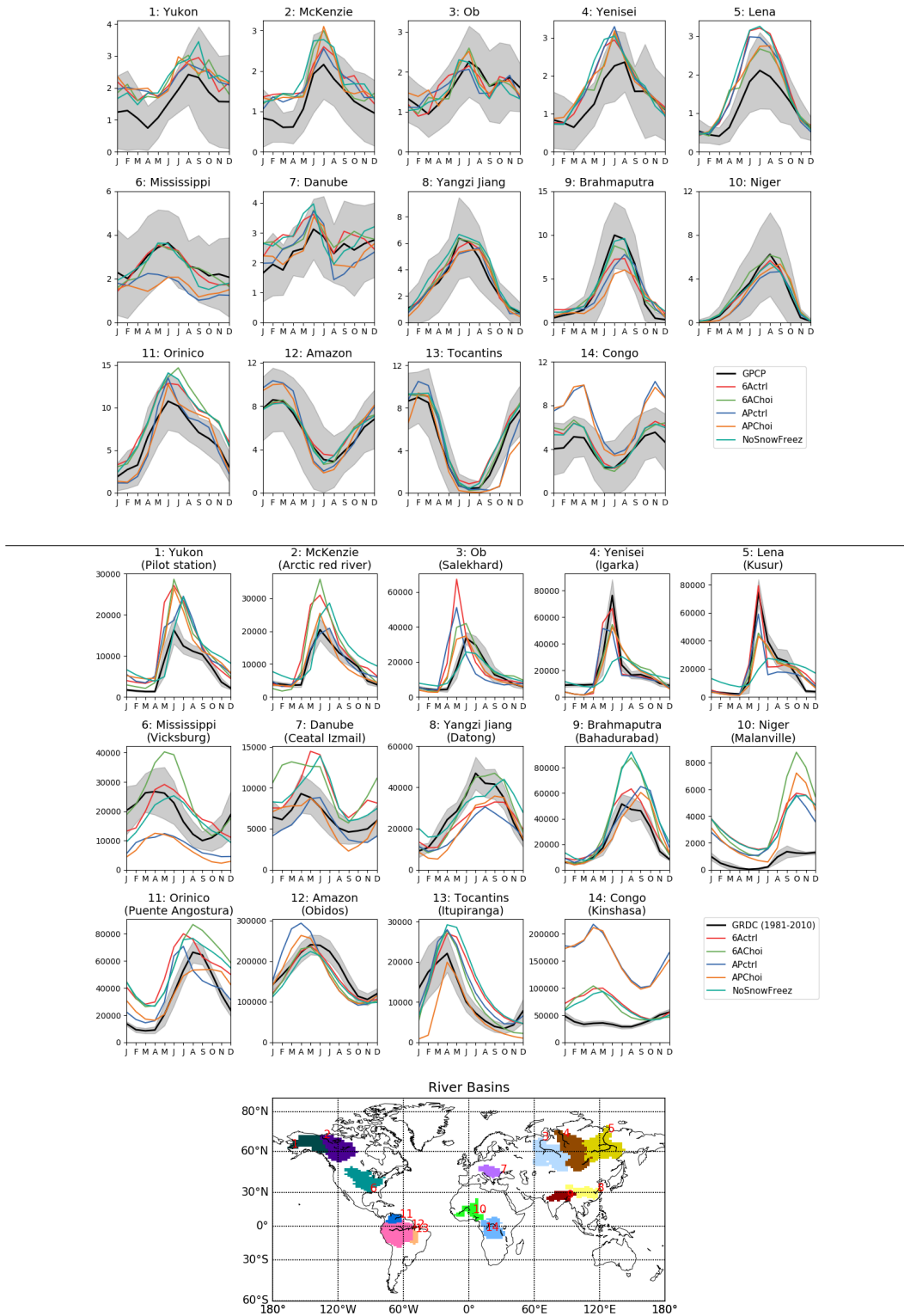


Figure 13. Multi-annual mean seasonal cycle of the precipitation (upper panel) and of river discharge (lower panel) observed and simulated for 14 major river basins and for the four reference experiments: 6Actrl, Choi6A, APctrl and ChoiAP and for the "NoSnowFreez" experiment described in table 2. The observations refer to the GPCP product for precipitation and to the Global Runoff Data Center (GRDC) database for the river discharges (Milliman & Farnsworth, 2011). The gray shaded areas indicate the interannual variability of the observed precipitation in the basin area (upper panel) and the interannual variability of the river discharge at the measurement stations.

- 820 • The improvement of the radiative balance and in particular the surface downward
821 SW radiation allows to reduce several temperature biases, some of which were shared
822 by many models that participated in the CMIP5 exercise (e.g. summer bias in mid-
823 latitudes; (Stouffer et al., 2017)). This confirms the essential role of the radiation
824 and its interactions with clouds for continental climates.
- 825 • The temperature in the surface layer of the polar regions is significantly improved
826 thanks to the refined turbulent diffusion scheme for stable situations and to the
827 new LW radiative scheme in LMDZ version 6A (Vignon et al., 2018). The boreal
828 regions respond with a slightly excessive reduction of the daily minimum temper-
829 ature while in CMIP5, several models including LMDZ shared a warm bias (Wei
830 et al., 2017). A more detailed consideration of the turbulent mixing linked to the
831 subgrid orography or high vegetation may help to partially compensate for this
832 cooling, but further tests and evaluation are necessary.
- 833 • With the exception of the surface albedo, the snow cover and to a lesser extent
834 the evaporation, the overall structure of the near surface biases is only marginally
835 sensitive to the land surface scheme whose impact is mostly relevant at regional
836 scale. However, for a given description of the atmospheric physics, the differences
837 induced by the change in LSM are statistically significant (at the 5% level) over
838 most of the continents for all variables examined but precipitation.
- 839 • The multi-layer hydrology gives a representation of the surface soil moisture in bet-
840 ter agreement with available observations than the Choi scheme and the quality
841 of evaporation in regions of strong coupling of the continental surface with the at-
842 mosphere is significantly improved.
- 843 • The snow scheme of intermediate complexity implemented in ORCHIDEE leads
844 to a better description of the snow cover on the continents. Mountainous regions
845 and in particular the Tibetan Plateau and High-mountain Asia remain challeng-
846 ing because radiative feedbacks and an imperfect description of the circulation in
847 these regions at regional scale induce a strong cold bias. Further refinements of
848 the snow scheme over complex terrains and of the atmospheric circulation are re-
849 quired to reduce these biases.
- 850 • The calculation of the fraction of frozen water in the soil implemented in the multi-
851 layer hydrology combined with the improved realism in volume and seasonality
852 of the precipitation simulated with the 6A version of LMDZ has improved the sea-
853 sonal cycle of rivers discharge in several major river basins.

854 Further developments based on the current version of the coupled atmosphere-land
855 continental surface system are also identified.

- 856 • The attempt to take into account sources of turbulent mixing such as orography-
857 induced small scales gravity-wave drag (Steenefeld et al., 2008) or the drag induced
858 by vertical obstacles penetrating the boundary layers such as trees needs to be fur-
859 ther refined.
- 860 • The benefit of using the dynamical roughness lengths as proposed by Massman
861 (1999) and tested locally by Su et al. (2001) over homogeneously vegetated sur-
862 faces (shrub, cotton, grass) has still to be thoroughly evaluated in the context of
863 the imperfect heterogeneous Land-Atmosphere coupling. In this context, the bulk
864 formulae for flux calculation use a unique value of the roughness length, aggre-
865 gated over possibly highly heterogeneous sub-grid surfaces, and a potentially wide
866 range of contrasting sub-grid surfaces sees the same boundary layer properties. The
867 development of more robust parameterizations for flux calculation over heteroge-
868 neous surfaces could benefit in the future from high-resolution simulations such
869 as Large Eddy Simulations.
- 870 • For CMIP6, even though it would have reduced an overall overestimation of the
871 evaporation, we considered it preferable not to activate the evaporation resistance
872 of the bare soil in its current state to avoid reinforcing a warm bias in summer that

would affect the quality of the simulations. Further work is needed to better calibrate the intensity of the evaporation resistance, which also impacts the ratio of transpiration to total evapotranspiration (T/ET), shown to exert a key influence on biophysical feedback strength in both present and future climates (Zeng et al., 2017). Owing to the number of intricated parametrizations in a climate model, such work cannot be done in isolation, and our results show that particular attention must be paid to the uncertainties of cloud parameterizations and cloud-radiation interactions.

- The multi-layer hydrology enables to consider new developments for the climate model. One of them is the introduction of realistic groundwater description, which may alleviate some biases by means of enhanced evapotranspiration owing to capillary rise from the water table (Campoy et al., 2013; F. Wang et al., 2018). The inclusion of irrigation in the simulations could also help reducing persistent biases (Puma & Cook, 2010), especially in places where it is fed by groundwater abstraction at non-renewable rates, like in India or the US Great Plains (Famiglietti, 2014; Al-Yaari et al., 2019).
- In the version of ORCHIDEE used for CMIP6, the soil freezing is diagnosed in each soil layer but the latent heat release/consumption associated with water freezing/thawing is not accounted for. This is, together with the better description of soil organic matter decomposition (Guimberteau et al., 2018) a preliminary step to account for the biogeochemical implications and positive feedback to global warming due to permafrost disappearance.
- Since the CMIP6 version, a description of the nitrogen cycle and its coupling to the carbon cycle has been implemented in ORCHIDEE (Vuichard et al., 2019). The impact of soil nitrogen availability (and more generally of soil nutrients) is crucial for plant growth but also for the energy and water cycle. Very recently we also included an ensemble of developments to improve the representation of forest dynamic and forest management with the inclusion of i) a new canopy radiative transfer scheme (2 streams model), ii) a new carbon allocation scheme based on observed allometric relationships, as well as iii) age and diameter classes and management practices (from natural to coppices). These developments described in Naudts et al. (2015) have a direct impact on the surface climate, changing the albedo of forest, the roughness length (varying with tree height dynamic), the latent and sensible heat fluxes and the overall surface temperature (see an application over Europe in Naudts et al. (2016)).
- Interestingly, none of the sensitivity tests to the surface processes described in this paper significantly impacted the TOA radiative budget, an essential target of the tuning of global climate models. This indicates that there is latitude for independent tuning for TOA radiation and for the land surface processes. Such an approach has not been adopted for the 6Actrl version of the IPSL-CM but it could improve the performance of the model and reduce some bias in future versions of the model (Li et al., 2019). The tuning of the free parameters is now recognized as necessary step in model development (Hourdin et al., 2017) that should not rule out the improvement of the physical content of parameterizations.

Acknowledgments

This work was supported by the DEPHY2 project funded by the French national program LEFE/INSU. The CMIP6 project at IPSL used the HPC resources of TGCC under the allocations 2016-A0030107732, 2017-R0040110492 and 2018-R0040110492 (project gencmip6) provided by GENCI. One of the authors (Y. Zhao) benefited from the French state aid managed by the ANR under the "Investissements d'avenir" programme with the reference ANR-11-IDEX-0004 - 17-EURE-0006. This study benefited from the ESPRI (Ensemble de Services Pour la Recherche l'IPSL) computing and data centre

925 (https://mesocentre.ipsl.fr) which is supported by CNRS, Sorbonne Universite, Ecole
 926 Polytechnique and CNES and through national and international grants Analysis pre-
 927 sented in 4.1 benefited from the support of the CMUG and ESA-CCI programs. The ver-
 928 sion of LMDZ and ORCHIDEE used for the production of CMIP6 will be made avail-
 929 able at the following address <http://www.lmd.jussieu.fr/~lmdz/pub>. In the ORCHIDEE
 930 community, the model is referred as "Orchidee Trunk" which is the official version de-
 931 veloped at IPSL. The version used for the specific simulations runs for this paper is the
 932 'svn' release 3427 in the
 933 *LMDZ6/branches/IPSLCM6.0.15* and the 'svn' release 5626 in the
 934 *tags/ORCHIDEE.2.0/ORCHIDEE_OL* branche. Simulations data used in the present
 935 paper will be made available with a DOI if the paper is accepted for publication.

936 Appendix A Gravity-wave and high-vegetation drag induced TKE

937 LMDZ deals with two effects of the sub-grid orography on the atmospheric flow:

- 938 1. the orographic blocking effect (called drag),
- 939 2. the orographic effect on the wind direction (called lift).

940 The drag and lift effects are described in Lott (1999). These two effects were modified
 941 during the tuning process. The drag and lift parameterizations (Lott & Miller, 1997) en-
 942 compass two processes: i) the 'blocking' of the flow leading to a flow separation at the
 943 relief flanks and ii) the orographic gravity-wave drag. The latter accounts for the drag
 944 due to wave breaking in the middle atmosphere as well as for the drag induced by low-
 945 level dissipation and breaking of trapped lee waves (Lott, 1998). The drag effect is cal-
 946 culated applying a local force opposed to the local flow, and it is used in all climate mod-
 947 els (Sandu et al., 2019). The lift effect is less widely used, and involves a force perpen-
 948 dicular to the local flow.

949 For the set-up of the sixth version of the model, the effect of the drag exerted by
 950 vegetation protruding into the first model layers has also been parameterized in LMDZ
 951 following Nepf (1999) and Masson & Seity (2009).

952 Orographic gravity-wave breaking and dissipation (e.g., Epifanio & Qian, 2008; Sun
 953 et al., 2015) as well as flow-canopy interactions (Finnigan, 2000) have been shown to be
 954 common paths to turbulence generation. More generally, every drag exerted on an air
 955 flow is associated to a loss of large scale kinetic energy and to an energy cascade from
 956 large scale kinetic energy to small scale turbulence (TKE) and ultimately to dissipation
 957 by molecular viscosity and conversion into enthalpy (Stull (1990), Sect. 5.3).

958 In LMDZ, any drag parameterization 'dg' calculates a wind tendency $[du/dt|_{dg}, dv/dt|_{dg}]$
 959 for all vertical levels in each atmospheric column. This tendency can be expressed as the
 960 vertical divergence of a momentum stress $(\overline{\rho\tilde{u}\tilde{w}}_{dg}, \overline{\rho\tilde{v}\tilde{w}}_{dg})$ viz:

$$\frac{\partial u}{\partial t}\Big|_{dg} = -\frac{1}{\rho} \frac{\partial \overline{\rho\tilde{u}\tilde{w}}_{dg}}{\partial z} \quad (\text{A1})$$

961

$$\frac{\partial v}{\partial t}\Big|_{dg} = -\frac{1}{\rho} \frac{\partial \overline{\rho\tilde{v}\tilde{w}}_{dg}}{\partial z} \quad (\text{A2})$$

962 where ρ is the air density and u and v are the zonal and meridional components
 963 of the wind vector respectively. The loss of kinetic energy k in an atmospheric layer as-
 964 sociated to the parameterized drag 'dg' thus reads:

$$\frac{\partial k}{\partial t}\Big|_{\text{dg}} = -\delta z \left[u \frac{\partial \overline{\rho \tilde{u} \tilde{w}}_{\text{dg}}}{\partial z} + v \frac{\partial \overline{\rho \tilde{v} \tilde{w}}_{\text{dg}}}{\partial z} \right] = \delta z \underbrace{\left[\overline{\rho \tilde{u} \tilde{w}}_{\text{dg}} \frac{\partial u}{\partial z} + \overline{\rho \tilde{v} \tilde{w}}_{\text{dg}} \frac{\partial v}{\partial z} \right]}_{\Gamma_K(z)} - \delta z \underbrace{\left[\frac{\partial u \overline{\rho \tilde{u} \tilde{w}}_{\text{dg}}}{\partial z} + \frac{\partial v \overline{\rho \tilde{v} \tilde{w}}_{\text{dg}}}{\partial z} \right]}_{\Psi(z)} \quad (\text{A3})$$

965 where δz is the depth of the considered atmospheric layer. We will see hereafter
 966 that Γ_K is an exchange term between large scale kinetic energy and TKE while Ψ cor-
 967 responds to the vertical divergence of power associated to the parametrized stress. Once
 968 integrated over a whole atmospheric column, as $\int_0^\infty \Psi dz = 0$, Eq. A3 reads:

$$\partial_t K|_{\text{dg}} = \int_0^\infty \partial_z u \overline{\rho \tilde{u} \tilde{w}} dz + \int_0^\infty \partial_z v \overline{\rho \tilde{v} \tilde{w}} dz \quad (\text{A4})$$

969 Where:

$$K = \int_0^\infty k dz = \int_0^\infty \rho \frac{(u^2 + v^2)}{2} dz \quad (\text{A5})$$

970 (Boville & Bretherton, 2003).

971 To guarantee energy conservation in LMDZ version 6A, $\partial_t K|_{\text{dg}}$ was initially cal-
 972 culated for each drag parameterization and then converted into enthalpy in each atmo-
 973 spheric column. To account for a more realistic mixing in the boundary-layer and to pre-
 974 clude artificial thermal decouplings over the continents, the loss of energy associated to
 975 the high-vegetation and orographic gravity-wave drag was then transferred to sub-grid
 976 TKE before being converted into enthalpy, thereby enhancing the mixing in the boundary-
 977 layer. Practically this is done as follows.

978 The parameterization of the vertical turbulent mixing in LMDZ version 6A is based
 979 on a local diffusion scheme combined with a mass-flux scheme for convective boundary
 980 layers, the so-called ‘thermal plume model’ (Hourdin et al., 2002; Rio et al., 2010). The
 981 local diffusion scheme is a 1.5 order closure K-gradient scheme developed by Yamada (1983)
 982 in which the diffusion coefficients depend on the TKE calculated with a prognostic equa-
 983 tion

$$\frac{\partial \text{TKE}}{\partial t} = \underbrace{\frac{1}{\rho} \frac{\partial}{\partial z} (\rho K_e \frac{\partial \text{TKE}}{\partial z})}_{\text{Turbulent diffusion}} - \underbrace{\overline{u'w'} \frac{\partial u}{\partial z} - \overline{v'w'} \frac{\partial v}{\partial z}}_{\text{Shear production}} + \underbrace{\frac{g}{\theta_v} \overline{w'\theta'_v}}_{\text{Buoyancy term}} - \underbrace{\frac{\text{TKE}^{3/2}}{c}}_{\text{Dissipation}} \quad (\text{A6})$$

984 where c is a real constant, θ_v the virtual potential temperature $\overline{u'w'}$ and $\overline{v'w'}$ the com-
 985 ponents of the turbulent momentum flux, $\frac{g}{\theta_v} \overline{w'\theta'_v}$ the buoyancy flux and K_e a turbulent
 986 diffusion coefficient.

987 The conversion of large scale energy into TKE due to the orographic gravity-wave
 988 drag and high-vegetation drag can therefore be taken into account by including the Γ_K
 989 terms associated to those parameterizations as additional ‘shear production’ terms into
 990 Eq. A6. For the vegetation, the drag coefficient is proportional to the fraction of pro-
 991 truding vegetation in the grid-box. More details and sensitivity tests can be found in Vignon
 992 (2017). One might also want to add the TKE tendency due to the flow-blocking com-
 993 ponent of the sub-grid orographic drag scheme. However the underlying physical mech-
 994 anism responsible for the energy cascade associated to flow blocking is not a priori ob-
 995 vious. This aspect deserves further investigation.

996 Appendix B A posteriori correction of the screen-level variables

997 B1 Diagnostics at the screen level

998 The calculation of the screen-level variables, tas (2m-temperature), huss (2m spec-
 999 ific humidity), uas and vas (eastward and northward surface wind) is done iteratively

1000 following Hess and McAvaney (1995). It is based on the Monin-Obukhov similarity the-
 1001 ory for the surface layer and the bulk formulation of the turbulent flux proposed by Louis
 1002 et al. (1982). The 2m-relative humidity, $hurs$, is then diagnosed from $hurs$ and the sat-
 1003 urated specific humidity at temperature tas .

1004 The wind, the temperature and the specific humidity profiles in the surface layer
 1005 follow equations:

$$\begin{cases} \frac{\kappa u}{u_*} = \ln\left(\frac{z}{z_{0m}}\right) - \Psi_M\left(\frac{z}{L}\right) \\ \frac{(\Theta - \Theta_s)}{\Theta_*} = \frac{1}{\kappa} \left(\ln\left(\frac{z}{z_{0h}}\right) - \Psi_H\left(\frac{z}{L}\right) + \Psi_H\left(\frac{z_{0h}}{L}\right) \right) \\ \frac{(q - q_{surf})}{q_*} = \frac{1}{\kappa} \left(\ln\left(\frac{z}{z_{0h}}\right) - \Psi_H\left(\frac{z}{L}\right) + \Psi_H\left(\frac{z_{0h}}{L}\right) \right) \end{cases} \quad (B1)$$

1006 with κ the empirical von Karman constant, L , the Monin-Obukhov length and Ψ , the
 1007 stability functions for the stability parameter $\zeta = \frac{z}{L}$. u_* is the friction velocity, Θ_* the
 1008 temperature scale and q_* the humidity scale. An empirical formulation for the stabil-
 1009 ity functions is given by Dyer (1974). According to the Monin-Obukhov theory, L , u_* ,
 1010 Θ_* and q_* are evaluated at the surface and are independent of z in the constant flux layer.
 1011 A first guess of the screen variables is estimated owing to eq. B1. Then the Louis bulk
 1012 formulation and the scale variables are used to calculate an updated value of the screen
 1013 level variables. In situations where the turbulence is vanishing and the atmosphere above
 1014 the surface is dry but the surface soil moisture is significantly above the residual value,
 1015 a wrong diagnostic of q_{surf} in ORCHIDEE led to inconsistencies in the stability diag-
 1016 nostics between the first-guess evaluation and the use of the Louis formulation. In such
 1017 conditions, the calculation can produce unrealistic (overestimated) values of tas up to
 1018 450K together with negative values of relative humidity. Luckily, apart from a few ex-
 1019 ceptional events, this occurs only one time a day at most. Thanks to that it was pos-
 1020 sible to a posteriori correct the screen level values for simulations for which the minimum
 1021 daily relative humidity was archived. In the vast majority of cases, these failures occur
 1022 in stable conditions. In such conditions $\Psi_H = -\frac{5z}{L}$ and one shows easily that Θ is a
 1023 monotonous function of z which implies that Θ is comprised between Θ_s , the surface tem-
 1024 perature and Θ_1 , the temperature at the first atmospheric level of the model. A simu-
 1025 lation where the screen level temperature is bounded at each timestep with the surface
 1026 and the air temperature at the first atmospheric level will then be used to validate the
 1027 a posteriori correction.

1028 B2 A posteriori correction for the screen-level variables

1029 The a posteriori reconstruction algorithm is described hereafter. The general idea
 1030 of the algorithm is to replace the erroneous values (daily maximum air temperature, tas -
 1031 max or surface daily minimum relative humidity, $hursmin$) by an interpolation between
 1032 the previous and the following day without failure. The rarity of the failure of the screen
 1033 variable calculation makes this approach feasible. The erroneous values (failure) are de-
 1034 tected by looking for negative values of $hursmin$.

- 1035 • Step 1: we detect possible failure by identifying all the grid points and days (of
 1036 index k) for which the estimated near surface humidity is negative.
- 1037 • Step 2: we correct the daily mean temperature by correcting the maximum in the
 1038 daily mean using information from the last and next day without failure as fol-
 1039 lows.

1040 For the derivation, we denote by T the 2m temperature, tas

1041 The daily average value will be noted $\bar{T} = \sum_1^N T_i / N$, where N is the number of
 1042 timesteps i within a day, and the maximum T_{max} . We introduce the daily max-
 1043 imum anomaly $D = T_{max} - \bar{T}$. We apply the interpolation in time between the
 1044 last (l) and next (n) day without failure to D , leading to the corrected value
 1045 $D^* = (1 - a)D_l + aD_n$ with $a = (k - l) / (n - l)$.

1046 Then we compute the corrected daily averaged temperature as \bar{T}^* noticing that

$$\bar{T}^* - \bar{T} = (T_{max}^* - T_{max}) / N = (\bar{T}^* - \bar{T} + D^* - D) / N \quad (B2)$$

1047 so that

$$\bar{T}^* = \bar{T} + (D^* - D)/(N - 1) \quad (\text{B3})$$

1048 • Step 3: we correct the maximum temperature from the corrected daily mean tem-
 1049 perature \bar{T}^* and interpolated daily anomaly D^* as

$$T_{max}^* = \bar{T}^* + D^* \quad (\text{B4})$$

1050 which can be written as well using Eq. B3 as

$$T_{max}^* = \bar{T} + (\bar{T}^* - \bar{T}) + D^* = \bar{T} + \frac{ND^* - D}{N - 1} \quad (\text{B5})$$

1051 For the daily values of tas, this approach leads to replacing a potential error of about
 1052 $\frac{1}{96} \times 150\text{K}$ (for a maximum error of 150K on the instantaneous value of the temperature,
 1053 96 being the number of timesteps in one day for LMDZ version 6) by an uncertainty of
 1054 at most $\frac{1}{96}$ of the daily maximum anomaly (that is about $\frac{10\text{K}}{96}$), that is more than 10 times
 1055 less. For tasmax the reconstruction procedure avoids creating extremes based on erro-
 1056 neous (and unrealistic) screen variable values.

1057 A similar 3-step approach is applied to correcting the relative humidity but tak-
 1058 ing as an information from the last and previous day without failure, the ratio $R = \frac{RH_{min}}{RH}$,
 1059 so that the procedure reads:

- 1060 • Step 1: Same as for T
- 1061 • Step 2: We apply the interpolation in time between the last (l) and next (n) day
 1062 without failure to R , leading to the corrected value
 1063 $R^* = (1 - a)R_l + aR_n$ with $a = (k - l)/(n - l)$. Then we compute the corrected
 1064 daily averaged relative humidity as \overline{RH}^* noticing that

$$\overline{RH}^* - \overline{RH} = (RH_{min}^* - RH_{min})/N = \frac{R^* \overline{RH}^* - RH_{min}}{N} \quad (\text{B6})$$

1065 and the corrected values are calculated with the following equations.

$$\overline{RH}^* = \frac{(\overline{RH} - \frac{RH_{min}}{N})}{(1 - \frac{R^*}{N})} \quad (\text{B7})$$

- 1066 • Step 3: we correct the minimum relative humidity from the corrected daily mean
 1067 relative humidity \overline{RH}^* and interpolated ratio R^* as

$$RH_{min}^* = R^* * \overline{RH}^* \quad (\text{B8})$$

1068 **B3 Evaluation of the uncertainty relying on the a posteriori correction**

1069 The a posteriori reconstruction (hereafter called OFF) is evaluated against the re-
 1070 sults of the near-surface temperature diagnosed on-line in the model (hereafter called ON)
 1071 and bounded at each timestep with the surface and the air temperature at the first at-
 1072 mospheric level. In the ON experiment the bounding is applied only for diagnostic pur-
 1073 pose and does not affect the behaviour of the model.

1074 For each grid point and each day of the 36 years of an AMIP experiment, the re-
 1075 construction error is evaluated with the difference between the OFF and the ON exper-
 1076 iments.

1077 Figure B1 shows the cumulated histogram of reconstruction errors with the a pos-
 1078 teriori method and the ON bounding method for the daily mean and maximum daily
 1079 temperature. For the majority of grid points and days, the OFF and ON methods give
 1080 similar results. The reconstruction error lies within the range (-0.2K, 0.4K). These small

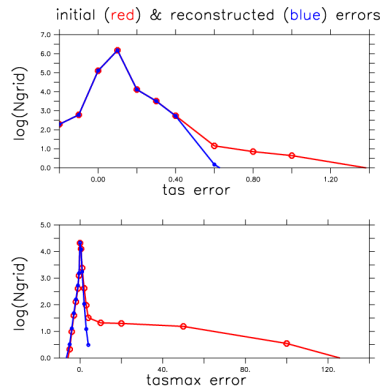


Figure B1. Cumulated histogram of the reconstruction errors for daily 2m-t. The y-axis is logarithmic. The red curve corresponds to the difference between the daily mean obtained with the original run and with the instantaneous values bounded with the surface and first atmospheric level temperature (ON experiment). The blue curve corresponds to the a posteriori correction.

1081 differences between the two methods for daily values show that the near-surface temper-
 1082 ature is not fundamentally modified by the OFF correction compared to what would be
 1083 obtained with an on-line correction. The reconstruction errors for the monthly mean near-
 1084 surface temperature would have been negligible compared to the daily errors, being 30
 1085 times smaller than daily errors.

1086 References

- 1087 Adler, R., Huffman, G., Chang, A., Ferraro, R., Xie, P., Janowiak, B., J. and Rudolf,
 1088 ... Arkin, P. (2003). The version 2 global precipitation climatology project
 1089 (gpcp) monthly precipitation analysis (1979-present). *J. Hydrometeorol.*, *4*,
 1090 1147-1167.
- 1091 Aït-Mesbah, S., Dufresne, J. L., Cheruy, F., & Hourdin, F. (2015, sep). The role
 1092 of thermal inertia in the representation of mean and diurnal range of sur-
 1093 face temperature in semiarid and arid regions. *GRL*, *42*, 7572-7580. doi:
 1094 10.1002/2015GL065553
- 1095 Al-Yaari, A., Ducharne, A., Cheruy, F., Crow, W. T., & Wigneron, J.-P. (2019).
 1096 Satellite-based soil moisture provides missing link between summertime precip-
 1097 itation and surface temperature biases in cmip5 simulations over conterminous
 1098 united states. *Scientific Reports*, *9*. doi: DOI:10.1038/s41598-018-38309-5
- 1099 Arnell, N. W., & Gosling, S. N. (2013). The impacts of climate change on river flow
 1100 regimes at the global scale. *Journal of Hydrology*, *486*, 351 - 364. doi: https://
 1101 doi.org/10.1016/j.jhydrol.2013.02.010
- 1102 Betts, A. K., Ball, J. H., Beljaars, A. C. M., Miller, M. J., & Viterbo, P. A. (1996).
 1103 The land surface-atmosphere interaction: A review based on observational and
 1104 global modeling perspectives. *Journal of Geophysical Research: Atmospheres*,
 1105 *101*(D3), 7209-7225. doi: 10.1029/95JD02135
- 1106 Boé, J. (2013). Modulation of soil moisture/precipitation interactions over france by
 1107 large scale circulation. *Clim Dyn*, *40*, 875-892. doi: 10.1007/s00382-012-1380
 1108 -6
- 1109 Boé, J., & Terray, L. (2008). Uncertainties in summer evapotranspiration changes
 1110 over europe and implications for regional climate change. *Geophys. Res. Lett.*,
 1111 *35*, L05702. doi: 10.1029/2007GL032417
- 1112 Bontemps, S., Boettcher, M., Brockmann, C., Kirches, G., Lamarche, C., Radoux,

- 1113 J., ... Defourny, P. (2015). Multi-year global land cover mapping at 300 m
 1114 and characterization for climate modelling : Achievements of the land cover
 1115 component of the esa climate change initiative. In *Int. arch. photogramm.*
 1116 *remote sens. spat. inf. sci.* (p. 323-328).
- 1117 Boone, A., & Etchevers, P. (2001). An intercomparison of three snow schemes of
 1118 varying complexity coupled to the same land surface model: Local-scale eval-
 1119 uation at an alpine site. *Journal of Hydrometeorology*, 2(4), 374-394. doi:
 1120 10.1175/1525-7541(2001)002<0374:AIOTSS>2.0.CO;2
- 1121 Boucher, O., Servonnat, J., & Co-authors, . (2020). Presentation and evaluation
 1122 of the ipsl-cm6a-lr climate model. *Journal of Advances in Modeling Earth Sys-*
 1123 *tems.*
- 1124 Boville, B. A., & Bretherton, C. S. (2003, December). Heating and Kinetic Energy
 1125 Dissipation in the NCAR Community Atmosphere Model. *J Clim*, 16, 3877-
 1126 3887. doi: 10.1175/1520-0442
- 1127 Campoy, A., Ducharne, A., Cheruy, F., Hourdin, F., Polcher, J., & Dupont,
 1128 J. C. (2013). Response of land surface fluxes and precipitation to different
 1129 soil bottom hydrological conditions in a general circulation model. *Jour-*
 1130 *nal of Geophysical Research: Atmospheres*, 118(19), 10,725–10,739. doi:
 1131 10.1002/jgrd.50627
- 1132 Chalita, S., & Le Treut, H. (1994, September). The albedo of temperate and boreal
 1133 forest and the Northern Hemisphere climate: a sensitivity experiment using the
 1134 LMD GCM. *Climate Dynamics*, 10, 231-240. doi: 10.1007/BF00208990
- 1135 Cheruy, F., Campoy, A., Dupont, J.-C., Ducharne, A., Hourdin, F., Haeffelin, M.,
 1136 ... Idelkadi, A. (2013). Combined influence of atmospheric physics and soil
 1137 hydrology on the simulated meteorology at the sirta atmospheric observatory.
 1138 *Clim. Dyn.*, 2251 2269. doi: 10.1007/s00382-012-1469-y
- 1139 Cheruy, F., Dufresne, J. L., Ait Mesbah, S., Grandpeix, J. Y., & Wang, F.
 1140 (2017). Role of soil thermal inertia in surface temperature and soil moisture-
 1141 temperature feedback. *Journal of Advances in Modeling Earth Systems*, 9(8),
 1142 2906–2919. Retrieved from <http://dx.doi.org/10.1002/2017MS001036> doi:
 1143 10.1002/2017MS001036
- 1144 Cheruy, F., Dufresne, J. L., Hourdin, F., & Ducharne, A. (2014). Role of clouds
 1145 and land-atmosphere coupling in midlatitude continental summer warm biases
 1146 and climate change amplification in cmip5 simulations. *Geophysical Research*
 1147 *Letters*, 41(18), 6493–6500. Retrieved from [http://dx.doi.org/10.1002/](http://dx.doi.org/10.1002/2014GL061145)
 1148 [2014GL061145](http://dx.doi.org/10.1002/2014GL061145) doi: 10.1002/2014GL061145
- 1149 Coindreau, O., Hourdin, F., Haeffelin, M., Mathieu, A., & Rio, C. (2007). As-
 1150 sessment of physical parametrizations using a global climate model with
 1151 strctchable grid and nudging. *Mon Weather Rev*, 135, 1474-1490. (doi:
 1152 10.1175/MWR3338.1)
- 1153 Dee, D., Uppala, S., Simmons, A., Berrisford, P., Poli, P., Kobayashi, S., ... others
 1154 (2011). The ERA-Interim reanalysis: Configuration and performance of the
 1155 data assimilation system. *Q J R Meteorol Soc*, 137(656), 553–597.
- 1156 De Rosnay, P., Polcher, J., Bruen, M., & Laval, K. (2002). Impact of a physically
 1157 based soil water flow and soil-plant interaction representation for modeling
 1158 large-scale land surface processes. *Journal of Geophysical Research*, 107(D11),
 1159 4118.
- 1160 Diallo, F. B., Hourdin, F., Rio, C., Traore, A.-K., Mellul, L., Guichard, F., & Ker-
 1161 goat, L. (2017). The surface energy budget computed at the grid-scale of
 1162 a climate model challenged by station data in west africa. *Journal of Ad-*
 1163 *vances in Modeling Earth Systems*, 9(7), 2710-2738. Retrieved from [https://](https://agupubs.onlinelibrary.wiley.com/doi/abs/10.1002/2017MS001081)
 1164 agupubs.onlinelibrary.wiley.com/doi/abs/10.1002/2017MS001081 doi:
 1165 10.1002/2017MS001081
- 1166 d'Orgeval, T., Polcher, J., & de Rosnay, P. (2008). Sensitivity of the West African
 1167 hydrological cycle in ORCHIDEE to infiltration processes. *Hydrol. Earth Syst.*

- 1168 *Sci*, 12, 1387–1401.
- 1169 Dorigo, W., Wagner, W., Albergel, C., Albrecht, F., Balsamo, G., Brocca, L., ...
 1170 Lecomte, P. (2017, 07). Esa cci soil moisture for improved earth system
 1171 understanding: State-of-the art and future directions. *Remote Sensing of*
 1172 *Environment*.
- 1173 Ducoudré, N., Laval, K., & Perrier, A. (1993). Sechiba, a new set of parameteriza-
 1174 tions of the hydrologic exchanges at the land-atmosphere interface within the
 1175 lmd atmospheric general circulation model. *Journal of Climate*, 248-273.
- 1176 Dyer, A. J. (1974). A review of flux-profile relationships. *Boundary-Layer Meteorol*,
 1177 7, 363-372. doi: 10.1007/BF00240838
- 1178 Eltahir, E. A. B. (1998). A soil moisture-rainfall feedback mechanism: 1. theory
 1179 and observations. *Water Resources Research*, 34(4), 765-776. Retrieved from
 1180 <https://agupubs.onlinelibrary.wiley.com/doi/abs/10.1029/97WR03499>
 1181 doi: 10.1029/97WR03499
- 1182 Eyring, V., Bony, S., Meehl, G. A., Senior, C. A., Stevens, B., Stouffer, R. J.,
 1183 & Taylor, K. E. (2016). Overview of the coupled model intercompari-
 1184 son project phase 6 (cmip6) experimental design and organization. *Geo-*
 1185 *scientific Model Development*, 9(5), 1937–1958. Retrieved from [https://](https://www.geosci-model-dev.net/9/1937/2016/)
 1186 www.geosci-model-dev.net/9/1937/2016/ doi: 10.5194/gmd-9-1937-2016
- 1187 Famiglietti, J. S. (2014). The global groundwater crisis. *Nature Climate Change*,
 1188 4(11), 945–948.
- 1189 Finnigan, J. (2000). Turbulence in plant canopies. *Annual Review of Fluid Mechan-*
 1190 *ics*, 32(1), 519-571. doi: 10.1146/annurev.fluid.32.1.519
- 1191 Garratt, J. R., & Hicks, B. B. (1973). Momentum, heat and water vapour transfer
 1192 to and from natural and artificial surfaces. *Quarterly Journal of the Royal Me-*
 1193 *teorological Society*, 99(422), 680–687. Retrieved from [http://dx.doi.org/10](http://dx.doi.org/10.1002/qj.49709942209)
 1194 [.1002/qj.49709942209](http://dx.doi.org/10.1002/qj.49709942209) doi: 10.1002/qj.49709942209
- 1195 Genthon, C., Six, D., Gallée, H., Grigioni, P., & Pellegrini, A. (2013). Two years of
 1196 atmospheric boundary layer observations on a 45-m tower at Dome C on the
 1197 Antarctic Plateau. *J Geophys Res Atmos*, 118. (doi:10.1002/jgrd.50128)
- 1198 Gouttevin, I., Krinner, G., Ciais, P., Polcher, J., & Legout, C. (2012). Multi-
 1199 scale validation of a new soil freezing scheme for a land-surface model
 1200 with physically-based hydrology. *The Cryosphere*, 6(2), 407–430. Re-
 1201 trieved from <https://www.the-cryosphere.net/6/407/2012/>
 1202 doi: 10.5194/tc-6-407-2012
- 1203 Guillod, B., Orlowsky, B., Miralles, D., Teuling, A. J., & Seneviratne, S. I. (2015).
 1204 Reconciling spatial and temporal soil moisture effects on afternoon rainfall.
 1205 *Nature Communication*, 6:6443. doi: 10.1038/ncomms7443
- 1206 Guimberteau, M., Drapeau, G., Ronchail, J., Sultan, B., Polcher, J., Martinez, J.-
 1207 M., ... Vauchel, P. (2012). Discharge simulation in the sub-basins of the
 1208 amazon using orchidee forced by new datasets. *Hydrology and Earth System*
 1209 *Sciences*, 16(3), 911–935. Retrieved from [https://www.hydrol-earth-syst](https://www.hydrol-earth-syst-sci.net/16/911/2012/)
 1210 [-sci.net/16/911/2012/](https://www.hydrol-earth-syst-sci.net/16/911/2012/) doi: 10.5194/hess-16-911-2012
- 1211 Guimberteau, M., Ducharne, A., Ciais, P., Boisier, J. P., Peng, S., De Weirdt,
 1212 M., & Verbeeck, H. (2014). Testing conceptual and physically based soil
 1213 hydrology schemes against observations for the amazon basin. *Geosci-*
 1214 *entific Model Development*, 7(3), 1115–1136. Retrieved from [https://](https://www.geosci-model-dev.net/7/1115/2014/)
 1215 www.geosci-model-dev.net/7/1115/2014/ doi: 10.5194/gmd-7-1115-2014
- 1216 Guimberteau, M., Laval, K., Perrier, A., & Polcher, J. (2012). Global effect of irri-
 1217 gation and its impact on the onset of the indian summer monsoon. *Clim. Dy-*
 1218 *namics*, 39, 1329. doi: 10.1007/s00382-011-1252-5
- 1219 Guimberteau, M., Zhu, D., Maignan, F., Huang, Y., Yue, C., Dantec-Nédélec, S.,
 1220 ... others (2018). Orchidee-mict (v8. 4.1), a land surface model for the high
 1221 latitudes: model description and validation. *Geoscientific Model Development*,
 1222 11(1), 121–163. Retrieved from <https://www.geosci-model-dev.net/11/>

- 1223 121/2018/ doi: 10.5194/gmd-11-121-2018
- 1224 Haarsma, R. J., Roberts, M. J., Vidale, P. L., Senior, C. A., Bellucci, A., Bao, Q.,
 1225 ... von Storch, J.-S. (2016). High resolution model intercomparison project
 1226 (highresmip v1.0) for cmip6. *Geoscientific Model Development*, 9(11), 4185–
 1227 4208. Retrieved from <https://www.geosci-model-dev.net/9/4185/2016/>
 1228 doi: 10.5194/gmd-9-4185-2016
- 1229 Harris, I., Jones, P., Osborn, T., & Lister, D. (2014). Updated high-resolution
 1230 grids of monthly climatic observations the cru ts3.10 dataset. *Interna-*
 1231 *tional Journal of Climatology*, 34(3), 623-642. Retrieved from [https://](https://rmets.onlinelibrary.wiley.com/doi/abs/10.1002/joc.3711)
 1232 rmets.onlinelibrary.wiley.com/doi/abs/10.1002/joc.3711 doi:
 1233 10.1002/joc.3711
- 1234 Hess, R., G. D. and Colman, & McAvaney, B. (1995). On computing screen temper-
 1235 atures, humidities and anemometer-height winds in large-scale models. *Aust.*
 1236 *Meteor. Mag.*, 44, 139-145.
- 1237 Hohenegger, C., Brockhaus, P., Bretherton, C., & Schär, C. (2009). The soil
 1238 moisture precipitation feedback in simulations with explicit and parameter-
 1239 ized convection. *Journal of Climate*, 22(19), 5003-5020. Retrieved from
 1240 <https://doi.org/10.1175/2009JCLI2604.1> doi: 10.1175/2009JCLI2604.1
- 1241 Hohenegger, C., & Stevens, B. (2018). The role of the permanent wilting point in
 1242 controlling the spatial distribution of precipitation. *Proceedings of the National*
 1243 *Academy of Sciences*. Retrieved from [http://www.pnas.org/content/early/](http://www.pnas.org/content/early/2018/05/10/1718842115)
 1244 [2018/05/10/1718842115](http://www.pnas.org/content/early/2018/05/10/1718842115) doi: 10.1073/pnas.1718842115
- 1245 Holton, J. R. (2004). *An introduction to dynamic meteorology*. Academic Press.
- 1246 Hourdin, F. (1992). *Etude et simulation numérique de la circulation générale des at-*
 1247 *mosphères planétaires (in french)* (Unpublished doctoral dissertation). Labora-
 1248 toire de Météorologie Dynamique, Paris, France.
- 1249 Hourdin, F., Couvreur, F., & Menut, L. (2002). Parameterization of the dry convec-
 1250 tive boundary layer based on a mass flux representation of thermals. *J Atmos*
 1251 *Sci*, 59, 1105-1123.
- 1252 Hourdin, F., Grandpeix, J.-Y., Rio, C., Bony, S., Jam, A., Cheruy, F., ... Roehrig,
 1253 R. (2013). LMDZ5B: the atmospheric component of the ipsl climate model
 1254 with revisited parameterizations for clouds and convection. *Climate Dynamics*,
 1255 40(9), 2193–2222. doi: 10.1007/s00382-012-1343-y
- 1256 Hourdin, F., Jam, C., A. and Rio, Couvreur, F., Sandu, I., Lefebvre, M.-P., Brient,
 1257 F., & Idelkadi, A. (2019). Unified parameterization of convective bound-
 1258 ary layer transport and clouds with the thermal plume model. *In revision in*
 1259 *JAMES*.
- 1260 Hourdin, F., Mauritsen, T., Gettelman, A., Golaz, J.-C., Balaji, V., Duan, Q.,
 1261 ... Williamson, D. (2017). The art and science of climate model tun-
 1262 ing. *Bulletin of the American Meteorological Society*, 98(3), 589-602.
 1263 Retrieved from <https://doi.org/10.1175/BAMS-D-15-00135.1> doi:
 1264 10.1175/BAMS-D-15-00135.1
- 1265 Hourdin, F., Musat, I., Bony, S., Braconnot, P., Codron, F., Dufresne, J.-L., ...
 1266 Lott, F. (2006). The LMDZ4 general circulation model: climate performance
 1267 and sensitivity to parametrized physics with emphasis on tropical convection.
 1268 *Climate Dynamics*, 27, 787-813. doi: 10.1007/s00382-006-0158-0
- 1269 Hourdin, F., Rio, C., Grandpeix, J., Madeleine, J., Cheruy, F., Rochetin, N., ...
 1270 Ghattas, J. (2020). Lmdz6a : the atmospheric component of the ipsl cli-
 1271 mate model with improved and better tuned physics. *Journal of Advances in*
 1272 *Modeling Earth Systems*.
- 1273 Hurtt, G., & Chini, S. e. a., L.P. and Frohling. (2011). Harmonization of land-use
 1274 scenarios for the period 15002100: 600 years of global gridded annual land-use
 1275 transitions, wood harvest, and resulting secondary lands. *Climatic Change*,
 1276 109(107). doi: 10.1007/s10584-011-0153-2
- 1277 Jaeger, E., & Seneviratne, S. (2011). Impact of soil moisture atmosphere coupling on

- 1278 european climate extremes and trends in a regional climate model. *Clim Dyn*,
1279 *36*, 1919-1939.
- 1280 Jakobson, E., Vihma, T., Palo, T., Jakobson, L., Keernik, H., & Jaagus, J. (2012).
1281 Validation of atmospheric reanalyses over the central arctic ocean. *Geophysical*
1282 *Research Letters*, *39*(10). Retrieved from [https://agupubs.onlinelibrary](https://agupubs.onlinelibrary.wiley.com/doi/abs/10.1029/2012GL051591)
1283 [.wiley.com/doi/abs/10.1029/2012GL051591](https://agupubs.onlinelibrary.wiley.com/doi/abs/10.1029/2012GL051591) doi: 10.1029/2012GL051591
- 1284 Jung, M., & Coauthors. (2011). Global patterns of land-atmosphere fluxes of carbon
1285 dioxide, latent heat, and sensible heat derived from eddy covariance, satel-
1286 lite, and meteorological observations. *J. Geophys. Res.*, *116*, G00J07. doi:
1287 10.1029/2010JG001566
- 1288 Jung, M., Reichstein, M., Margolis, H. A., Cescatti, A., Richardson, A. D., Arain,
1289 M. A., ... Williams, C. (2011). Global patterns of land-atmosphere fluxes of
1290 carbon dioxide, latent heat, and sensible heat derived from eddy covariance,
1291 satellite, and meteorological observations. *Journal of Geophysical Research:*
1292 *Biogeosciences*, *116*(G3), n/a–n/a. (G00J07) doi: 10.1029/2010JG001566
- 1293 Kato, S., Loeb, N. G., Rose, F. G., Doelling, D. R., Rutan, D. A., Caldwell, T. E.,
1294 ... Weller, R. A. (2013). Surface irradiances consistent with ceres-derived top-
1295 of-atmosphere shortwave and longwave irradiances. *J. Climate*, *26*, 2719-2740.
1296 doi: 10.1175/JCLI-D-12-00436.1.
- 1297 King, J. C., Connolley, W. M., & Derbyshire, S. H. (2001). Sensitivity of mod-
1298 elled antarctic climate to surface and boundarylayer flux parametrizations.
1299 *Quarterly Journal of the Royal Meteorological Society*, *127*(573), 779-794. Re-
1300 trieved from [https://rmets.onlinelibrary.wiley.com/doi/abs/10.1002/](https://rmets.onlinelibrary.wiley.com/doi/abs/10.1002/qj.49712757304)
1301 [qj.49712757304](https://rmets.onlinelibrary.wiley.com/doi/abs/10.1002/qj.49712757304) doi: 10.1002/qj.49712757304
- 1302 Klein, S. A., Jiang, X., Boyle, J., Malyshev, S., & Xie, S. (2006). Diagnosis of the
1303 summertime warm and dry bias over the u.s. southern great plains in the gfdl
1304 climate model using a weather forecasting approach. *Geophysical Research*
1305 *Letters*, *33*(18), n/a–n/a. Retrieved from [http://dx.doi.org/10.1029/](http://dx.doi.org/10.1029/2006GL027567)
1306 [2006GL027567](http://dx.doi.org/10.1029/2006GL027567) (L18805) doi: 10.1029/2006GL027567
- 1307 Koster, R., Dirmeyer, P., Guo, Z., Bonan, G., Chan, E., Cox, P., ... others (2004).
1308 Regions of strong coupling between soil moisture and precipitation. *Science*,
1309 *305*(5687), 1138.
- 1310 Koster, R. D., Guo, Z., Yang, R., Dirmeyer, P. A., Mitchell, K., & Puma, M. J.
1311 (2009). On the nature of soil moisture in land surface models. *Journal of*
1312 *Climate*, *22*(16), 4322-4335. Retrieved from [https://doi.org/10.1175/](https://doi.org/10.1175/2009JCLI2832.1)
1313 [2009JCLI2832.1](https://doi.org/10.1175/2009JCLI2832.1) doi: 10.1175/2009JCLI2832.1
- 1314 Kottek, M., Grieser, J., Beck, C., Rudolf, B., & Rubel, F. (2006). World map of the
1315 kppen-geiger climate classification updated. *Meteorol. Z.*, *15*, 259-263. doi: 10
1316 .1127/0941-2948/2006/0130
- 1317 Krishnan, R., Sabin, T. P., Madhura, R. K., Vellore, R. K., Mujumdar, M., Sanjay,
1318 J., ... Rajeevan, M. (2019, Apr 01). Non-monsoonal precipitation response
1319 over the western himalayayas to climate change. *Climate Dynamics*, *52*(7), 4091–
1320 4109. Retrieved from <https://doi.org/10.1007/s00382-018-4357-2> doi:
1321 10.1007/s00382-018-4357-2
- 1322 Laval, K. (1988). *Experience with surface processes at lmd. parameterization of*
1323 *fluxes over land surface* (Tech. Rep.).
- 1324 Le Quéré, C., Andrew, R. M., Friedlingstein, P., Sitch, S., Hauck, J., Pongratz, J.,
1325 ... others (2018). Global carbon budget 2018. *Earth System Science Data*,
1326 *10*(4), 2141–2194.
- 1327 Li, S., Rupp, D. E., Hawkins, L., Mote, P. W., McNeall, D., Sparrow, S. N., ...
1328 Wettstein, J. J. (2019). Reducing climate model biases by exploring pa-
1329 rameter space with large ensembles of climate model simulations and statis-
1330 tical emulation. *Geoscientific Model Development*, *12*(7), 3017–3043. Re-
1331 trieved from <https://www.geosci-model-dev.net/12/3017/2019/> doi:
1332 10.5194/gmd-12-3017-2019

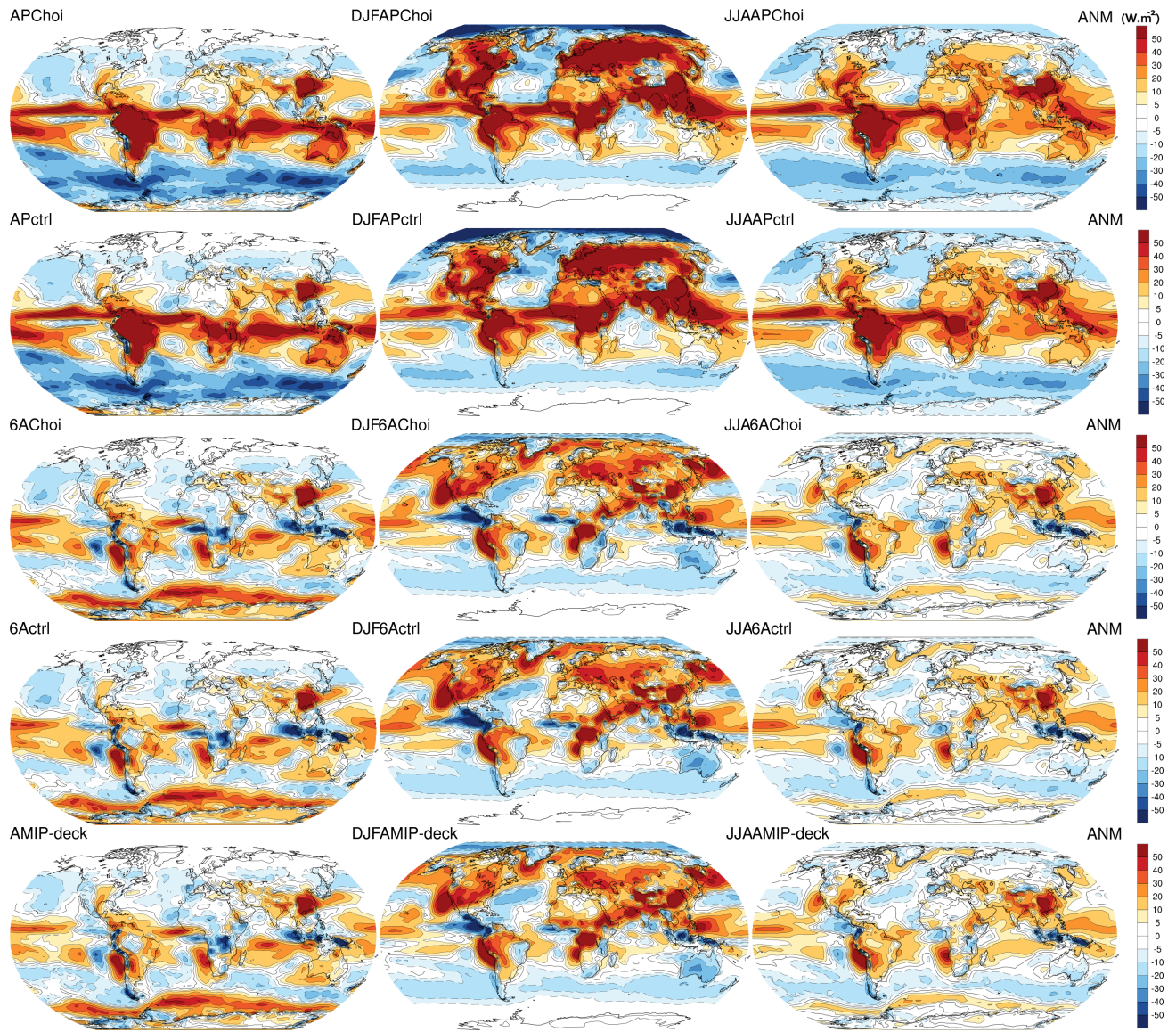
- 1333 Lindsay, R., Wensnahan, M., Schweiger, A., & Zhang, J. (2014). Evaluation of
 1334 seven different atmospheric reanalysis products in the arctic. *Journal of Cli-*
 1335 *mate*, 27(7), 2588-2606. Retrieved from [https://doi.org/10.1175/JCLI-D-](https://doi.org/10.1175/JCLI-D-13-00014.1)
 1336 [13-00014.1](https://doi.org/10.1175/JCLI-D-13-00014.1) doi: 10.1175/JCLI-D-13-00014.1
- 1337 Lott, F. (1998). Linear mountain drag and averaged pseudo-momentum flux profiles
 1338 in the presence of trapped lee waves. *Tellus*, 50A, 12-25.
- 1339 Lott, F. (1999). Alleviation of stationary biases in a gcm through a mountain drag
 1340 parametrization scheme and a simple representation of mountain lift forces.
 1341 *Mon Weath Rev*, 127, 788-800.
- 1342 Lott, F., & Miller, M. J. (1997). A new subgrid-scale orographic drag parametriza-
 1343 tion: Its formulation and testing. *Q J R Meteorol Soc*, 123, 101-127.
- 1344 Louis, J.-F., Tiedtke, M., & Geleyn, J.-F. (1982). A short history of the pbl param-
 1345 eterization at ecmwf. In *Workshop on planetary boundary layer parameteriza-*
 1346 *tion, 25-27 november 1981* (p. 59-79). Shinfield Park, Reading: ECMWF.
- 1347 Lurton, T., Balkanski, Y., Bastrikov, V., Bekki, S., Bopp, L., Braconnot, P.,
 1348 ... Boucher, O. (2020). Implementation of the cmip6 forcing data in
 1349 the ipsl-cm6a-lr model. *Journal of Advances in Modeling Earth Systems*,
 1350 12(4), e2019MS001940. Retrieved from [https://agupubs.onlinelibrary](https://agupubs.onlinelibrary.wiley.com/doi/abs/10.1029/2019MS001940)
 1351 [.wiley.com/doi/abs/10.1029/2019MS001940](https://agupubs.onlinelibrary.wiley.com/doi/abs/10.1029/2019MS001940) (e2019MS001940
 1352 10.1029/2019MS001940) doi: 10.1029/2019MS001940
- 1353 Malhi, Y. (1996). The behaviour of the roughness length for temperature over
 1354 heterogeneous surfaces. *Quarterly Journal of the Royal Meteorological So-*
 1355 *ciety*, 122(533), 1095-1125. Retrieved from [http://dx.doi.org/10.1002/](http://dx.doi.org/10.1002/qj.49712253305)
 1356 [qj.49712253305](http://dx.doi.org/10.1002/qj.49712253305) doi: 10.1002/qj.49712253305
- 1357 Manabe, S. (1969). Climate and the ocean circulation i. the atmospheric circulation
 1358 and the hydrology of the earth's surface. *Monthly Weather Review*, 97(11),
 1359 739-774.
- 1360 Martens, B., Miralles, D. G., Lievens, H., van der Schalie, R., de Jeu, R. A. M.,
 1361 Fernández-Prieto, D., ... Verhoest, N. E. C. (2017). Gleam v3: satellite-based
 1362 land evaporation and rootzone soil moisture. *Geoscientific Model Development*,
 1363 10(5), 1903-1925. Retrieved from [https://www.geosci-model-dev.net/10/](https://www.geosci-model-dev.net/10/1903/2017/)
 1364 [1903/2017/](https://www.geosci-model-dev.net/10/1903/2017/) doi: 10.5194/gmd-10-1903-2017
- 1365 Massman, W. (1999). A model study of kbh-1 for vegetated surfaces using "lo-
 1366 calized near-field" lagrangian theory. *Journal of Hydrology*, 223(1), 27 - 43.
 1367 Retrieved from [http://www.sciencedirect.com/science/article/pii/](http://www.sciencedirect.com/science/article/pii/S0022169499001043)
 1368 [S0022169499001043](http://www.sciencedirect.com/science/article/pii/S0022169499001043) doi: [https://doi.org/10.1016/S0022-1694\(99\)00104-3](https://doi.org/10.1016/S0022-1694(99)00104-3)
- 1369 Masson, V., & Seity, Y. (2009). Including atmospheric layers in vegetation and ur-
 1370 ban offline surface schemes. *Journal of Applied Meteorology and Climatology*,
 1371 48(7), 1377-1397. doi: 10.1175/2009JAMC1866.1
- 1372 Ménégos, M., Krinner, G., Balkanski, Y., Boucher, O., Cozic, A., Lim, S., ... Ja-
 1373 cobi, H. W. (2014). Snow cover sensitivity to black carbon deposition in
 1374 the himalayas: from atmospheric and ice core measurements to regional cli-
 1375 mate simulations. *Atmospheric Chemistry and Physics*, 14(8), 4237-4249.
 1376 Retrieved from <https://www.atmos-chem-phys.net/14/4237/2014/> doi:
 1377 10.5194/acp-14-4237-2014
- 1378 Milliman, J. D., & Farnsworth, K. L. (2011). *River discharge to the coastal*
 1379 *ocean: A global synthesis*. Cambridge University Press. doi: 10.1017/
 1380 CBO9780511781247
- 1381 Miralles, D., and. Chiel C. van Heerwaarden, A. J. T., & de Arellano, J. V.-G.
 1382 (2014). Mega-heatwave temperatures due to combined soil desiccation
 1383 and atmospheric heat accumulation. *Nature Geoscience*, 7, 756-761. doi:
 1384 10.1038/ngeo2141
- 1385 Mlawer, E. J., Taubman, S. J., Brown, P. D., Iacono, M. J., & Clough, S. A.
 1386 (1997). Radiative transfer for inhomogeneous atmospheres: Rrtm, a val-
 1387 idated correlated-k model for the longwave. *Journal of Geophysical Re-*

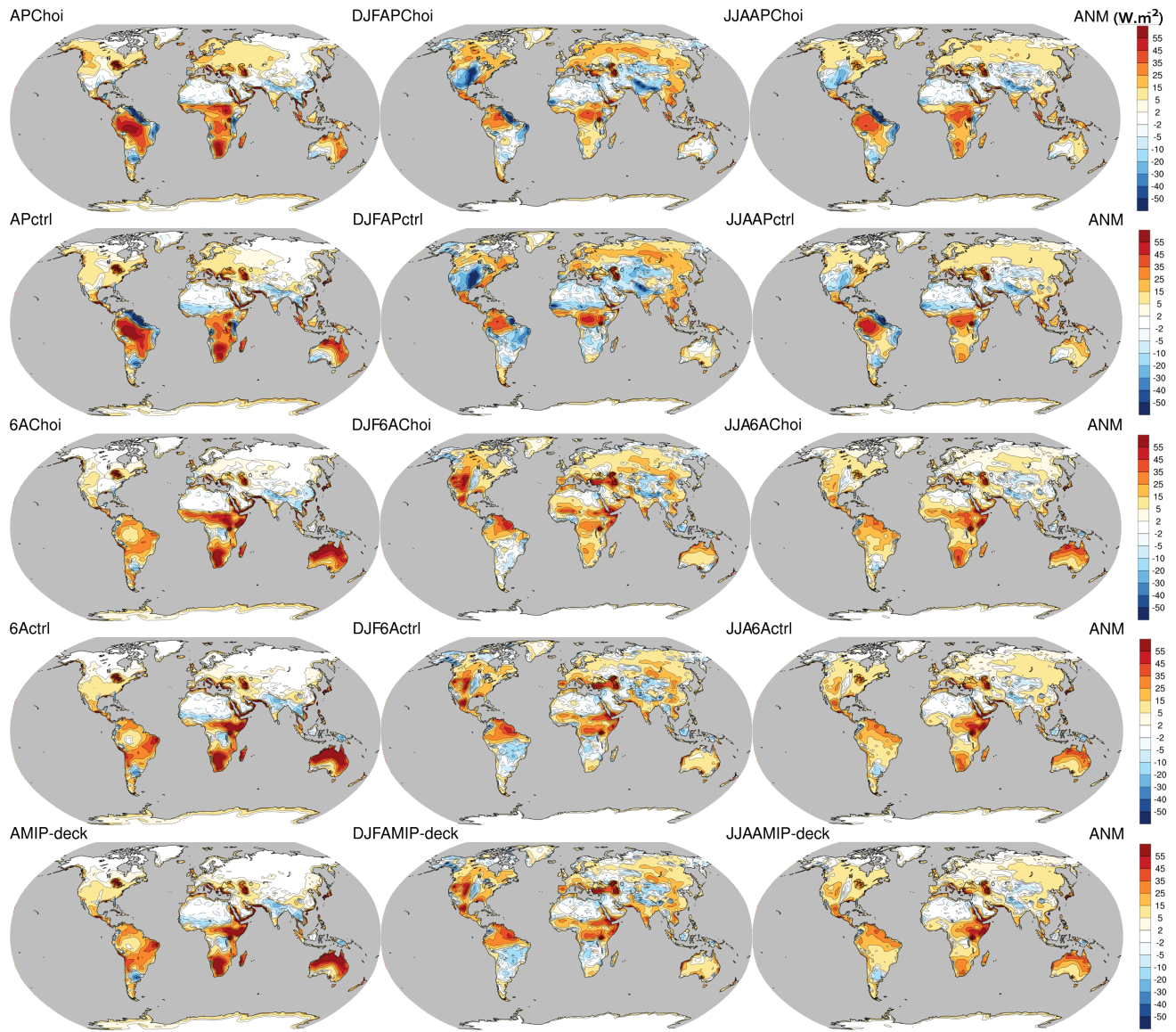
- 1388 search: *Atmospheres*, 102(D14), 16663-16682. Retrieved from [https://](https://agupubs.onlinelibrary.wiley.com/doi/abs/10.1029/97JD00237)
1389 agupubs.onlinelibrary.wiley.com/doi/abs/10.1029/97JD00237 doi:
1390 10.1029/97JD00237
- 1391 Morcrette, C. J., Van Weverberg, K., Ma, H.-Y., Ahlgrimm, M., Bazile, E., Berg,
1392 L. K., ... Petch, J. (2018). Introduction to causes: Description of weather and
1393 climate models and their near-surface temperature errors in 5-day hindcasts
1394 near the southern great plains. *Journal of Geophysical Research: Atmospheres*,
1395 n/a–n/a. Retrieved from <http://dx.doi.org/10.1002/2017JD027199>
1396 (2017JD027199) doi: 10.1002/2017JD027199
- 1397 Morcrette, J.-J. (1991). Radiation and cloud radiative properties in the european
1398 centre for medium range weather forecasts forecasting system. *Journal of Geo-*
1399 *physical Research: Atmospheres*, 96(D5), 9121-9132. Retrieved from [https://](https://agupubs.onlinelibrary.wiley.com/doi/abs/10.1029/89JD01597)
1400 agupubs.onlinelibrary.wiley.com/doi/abs/10.1029/89JD01597 doi: 10
1401 .1029/89JD01597
- 1402 Naudts, K., Chen, Y., McGrath, M. J., Ryder, J., Valade, A., Otto, J., & Luysaert,
1403 S. (2016). Europes forest management did not mitigate climate warming.
1404 *Science*, 351(6273), 597–600.
- 1405 Naudts, K., Ryder, J., McGrath, M., Otto, J., Chen, Y., Valade, A., ... others
1406 (2015). A vertically discretised canopy description for orchidee (svn r2290) and
1407 the modifications to the energy, water and carbon fluxes. *Geoscientific Model*
1408 *Development*, 8, 2035–2065.
- 1409 Nepf, H. M. (1999). Drag, turbulence, and diffusion in flow through emergent veg-
1410 etation. *Water Resources Research*, 35(2), 479-489. Retrieved from [https://](https://agupubs.onlinelibrary.wiley.com/doi/abs/10.1029/1998WR900069)
1411 agupubs.onlinelibrary.wiley.com/doi/abs/10.1029/1998WR900069 doi:
1412 10.1029/1998WR900069
- 1413 Peterson, B. J., Holmes, R. M., McClelland, J. W., Vörösmarty, C. J., Lammers,
1414 R. B., Shiklomanov, A. I., ... Rahmstorf, S. (2002). Increasing river dis-
1415 charge to the arctic ocean. *Science*, 298(5601), 2171–2173. Retrieved
1416 from <https://science.sciencemag.org/content/298/5601/2171> doi:
1417 10.1126/science.1077445
- 1418 Polcher, J. (2003). *Les processus de surface lchelle globale (in french)* (Unpublished
1419 doctoral dissertation). HDR, Université Pierre et Marie, Curie, France.
- 1420 Puma, M., & Cook, B. (2010). Effects of irrigation on global climate during the 20th
1421 century. *Journal of Geophysical Research: Atmospheres*, 115(D16).
- 1422 Reeves Eyre, J. E. J., & Zeng, X. (2017). Evaluation of greenland near surface air
1423 temperature datasets. *The Cryosphere*, 11(4), 1591–1605. doi: 10.5194/tc-11
1424 -1591-2017
- 1425 Rio, C., Hourdin, F., Couvreur, F., & Jam, A. (2010). Resolved versus parametrized
1426 boundary-layer plumes. Part II: continuous formulations of mixing rates for
1427 mass-flux schemes. *Boundary-layer Meteorol.* (Doi:10.1007/s10546-010-9478)
- 1428 Rio, C., Hourdin, J., F. Grandpeix, & Lafore, J. (2009). Shifting the diurnal
1429 cycle of parametrized deep convection over land. *J Geophys Res.* (doi:
1430 10.1029/2008GL036779)
- 1431 Robinson, D. A., Estilow, T. W., & Program, N. C. (2012). Noaa climate data
1432 record (cdr) of northern hemisphere (nh) snow cover extent (sce), version 1,
1433 2019-07-03t18:47:12z.
1434 doi: 10.7289/V5N014G9
- 1435 Rochetin, N., Couvreur, F., Grandpeix, J.-Y., & Rio, C. (2014). Deep convection
1436 triggering by boundary layer thermals. part i: Les analysis and stochastic
1437 triggering formulation. *Journal of the Atmospheric Sciences*, 71(2), 496-
1438 514. Retrieved from <https://doi.org/10.1175/JAS-D-12-0336.1> doi:
1439 10.1175/JAS-D-12-0336.1
- 1440 Rochetin, N., Grandpeix, J.-Y., Rio, C., & Couvreur, F. (2014). Deep convection
1441 triggering by boundary layer thermals. part ii: Stochastic triggering param-
1442 eterization for the lmdz gcm. *Journal of the Atmospheric Sciences*, 71(2),

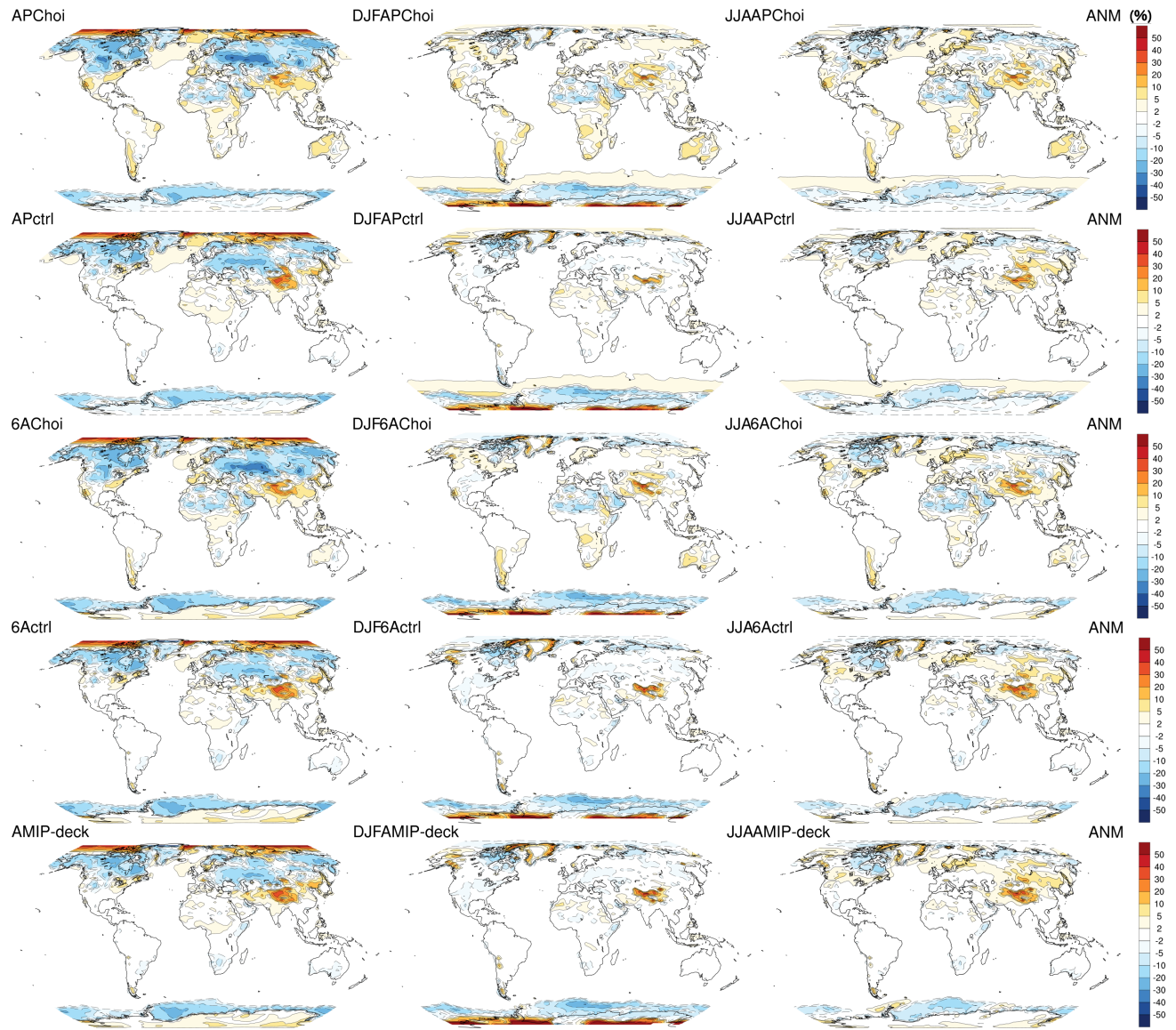
- 1443 515-538. Retrieved from <https://doi.org/10.1175/JAS-D-12-0337.1> doi:
1444 10.1175/JAS-D-12-0337.1
- 1445 Roehrig, R., Bouniol, D., Guichard, F., Hourdin, F., & Redelsperger, J.-L. (2013).
1446 The present and future of the west african monsoon: A process-oriented as-
1447 sessment of cmip5 simulations along the amma transect. *Journal of Cli-*
1448 *mate*, 26(17), 6471-6505. Retrieved from <https://doi.org/10.1175/>
1449 [JCLI-D-12-00505.1](https://doi.org/10.1175/JCLI-D-12-00505.1) doi: 10.1175/JCLI-D-12-00505.1
- 1450 Sabin, T. P., Krishnan, R., Ghattas, J., Denvil, S., Dufresne, J.-L., Hourdin,
1451 F., & Pascal, T. (2013, Jul 01). High resolution simulation of the south
1452 asian monsoon using a variable resolution global climate model. *Climate*
1453 *Dynamics*, 41(1), 173-194. Retrieved from <https://doi.org/10.1007/>
1454 [s00382-012-1658-8](https://doi.org/10.1007/s00382-012-1658-8) doi: 10.1007/s00382-012-1658-8
- 1455 Sandu, I., Beljaars, A., Bechtold, P., Mauritsen, T., & Balsamo, G. (2013). Why
1456 is it so difficult to represent stably stratified conditions in numerical weather
1457 prediction (nwp) models? *Journal of Advances in Modeling Earth Systems*,
1458 5(2), 117-133. Retrieved from <http://dx.doi.org/10.1002/jame.20013>
1459 doi: 10.1002/jame.20013
- 1460 Sandu, I., van Niekerk, A., Shepherd, T. G., Vosper, S. B., Zadra, A., Bacmeis-
1461 ter, J., ... Svensson, G. (2019). Impacts of orography on large-scale at-
1462 mospheric circulation. *npj Climate and Atmospheric Science*, 2, 1-8. doi:
1463 <https://doi.org/10.1038/s41612-019-0065-9>
- 1464 Schär, L., C. and D., U., B., & E., H. (1999). The soil-precipitation feedback: A pro-
1465 cess study with a regional climate model. *J. Climate*, 12, 722-741.
- 1466 Schewe, J., Heinke, J., Gerten, D., Haddeland, I., W., A., Clark, D., ... Kabat, P.
1467 (2014). Multimodel assessment of water scarcity under climate change. *PNAS*,
1468 111(9), 3245-3250. doi: 10.1073/pnas.1222460110
- 1469 Sellers, P. J., Mintz, Y., Sud, Y. C., & Dalcher, A. (1986). A simple bio-
1470 sphere model (sib) for use within general circulation models. *Journal*
1471 *of the Atmospheric Sciences*, 43(6), 505-531. Retrieved from [https://](https://doi.org/10.1175/1520-0469(1986)043<0505:ASBMFU>2.0.CO;2)
1472 [doi.org/10.1175/1520-0469\(1986\)043<0505:ASBMFU>2.0.CO;2](https://doi.org/10.1175/1520-0469(1986)043<0505:ASBMFU>2.0.CO;2) doi:
1473 10.1175/1520-0469(1986)043<0505:ASBMFU>2.0.CO;2
- 1474 Seneviratne, S., Nicolls, N., Easterling, D., Goodess, C., Kanae, S., Kossin, J., ...
1475 Zhang, X. (2012). Managing the risks of extreme events and disasters to ad-
1476 vance climate change adaptation. In C. Field et al. (Eds.), *A special report of*
1477 *working groups i and ii of the intergovernmental panel on climatechange (ipcc)*
1478 (p. 109-230). Cambridge University Press, Cambridge, United Kingdom and
1479 New York, NY, USA.
- 1480 Seneviratne, S. I., Corti, T., Davin, E. L., Hirschi, M., Jaeger, E. B., Lehner, I., ...
1481 Teuling, A. J. (2010). Investigating soil moisture climate interactions in a
1482 changing climate: A review. *Earth-Science Reviews*, 99(3-4), 125 - 161. doi:
1483 10.1016/j.earscirev.2010.02.004
- 1484 Steeneveld, G. J., Holtslag, A. A. M., Nappo, C. J., van de Wiel, B. J. H., & Mahrt,
1485 L. (2008). Exploring the possible role of small-scale terrain drag on stable
1486 boundary layers over land. *Journal of Applied Meteorology and Cli-*
1487 *matology*, 47(10), 2518-2530. Retrieved from <https://doi.org/10.1175/>
1488 [2008JAMC1816.1](https://doi.org/10.1175/2008JAMC1816.1) doi: 10.1175/2008JAMC1816.1
- 1489 Stouffer, R. J., Eyring, V., Meehl, G. A., Bony, S., Senior, C., Stevens, B., &
1490 Taylor, K. E. (2017). C mip5 scientific gaps and recommendations for
1491 cmip6. *Bulletin of the American Meteorological Society*, 98(1), 95-105.
1492 Retrieved from <https://doi.org/10.1175/BAMS-D-15-00013.1> doi:
1493 10.1175/BAMS-D-15-00013.1
- 1494 Stull, R. B. (1990). *An introduction to boundary layer meteorology*. Kluwer, Boston.
- 1495 Su, Z., Schumge, T., Kustas, W. P., & Massman, W. J. (2001). An evalua-
1496 tion of two models for estimation of the roughness height for heat transfer
1497 between the land surface and the atmosphere. *Journal of Applied Mete-*

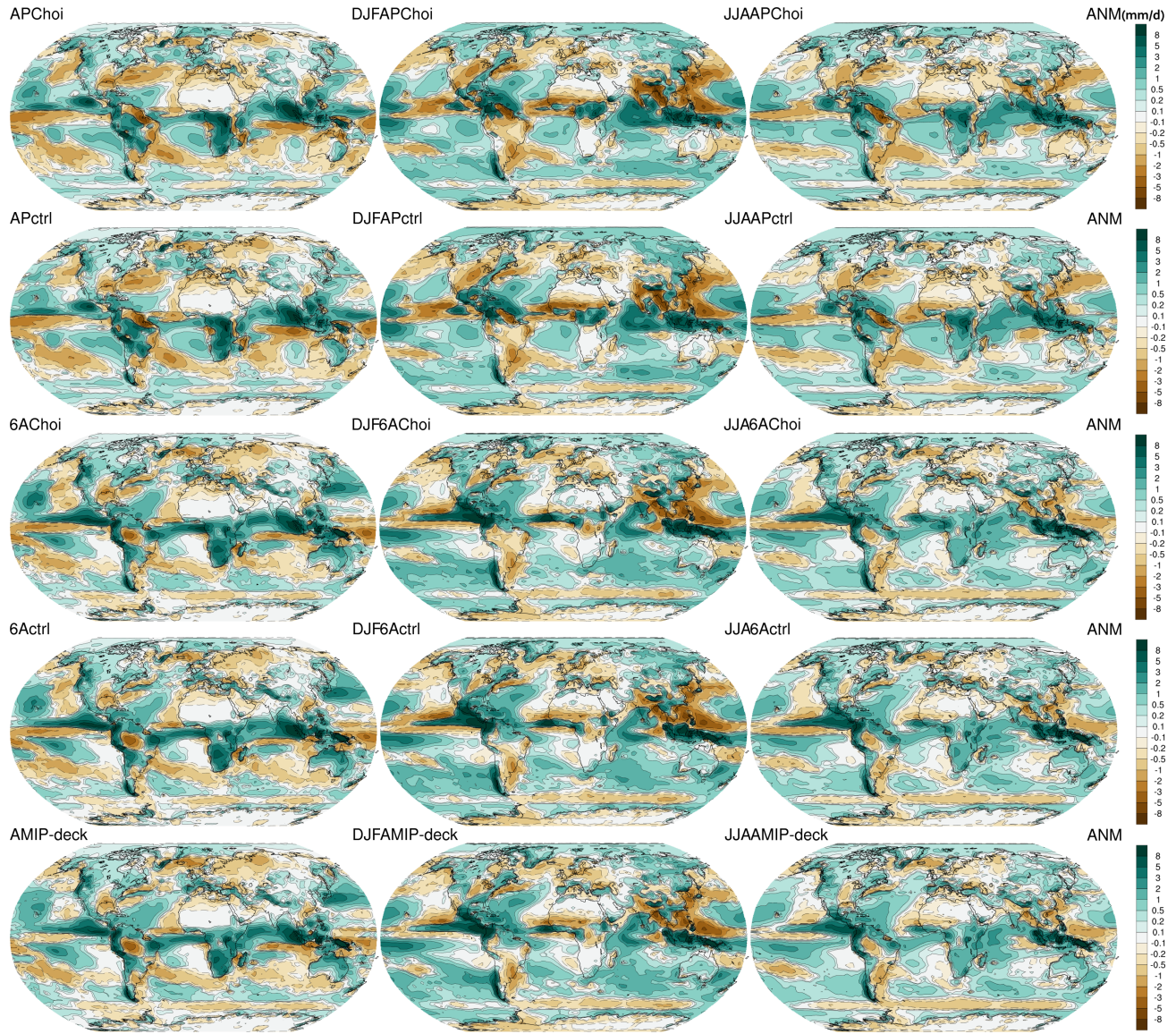
- 1498 *orology*, 40(11), 1933-1951. Retrieved from [https://doi.org/10.1175/](https://doi.org/10.1175/1520-0450(2001)040<1933:AEOTMF>2.0.CO;2)
1499 1520-0450(2001)040<1933:AEOTMF>2.0.CO;2 doi: 10.1175/1520-0450(2001)
1500 040<1933:AEOTMF>2.0.CO;2
- 1501 Taylor, C. M., de Jeu, R. A. M., Guichard, F., Harris, P. P., & Dorigo, W. A. (2012,
1502 Sep). Afternoon rain more likely over drier soils. *Nature*, 4, 423-426. doi: 10
1503 .1038/nature11377
- 1504 Taylor, C. M., Gounou, A., Guichard, F., Harris, P. P., Ellis, R. J., Couvreur, F.,
1505 & de Kauwe, M. (2011, jul). Frequency of Sahelian storm initiation enhanced
1506 over mesoscale soil-moisture patterns. *Nature Geoscience*, 4, 430-433. doi:
1507 10.1038/ngeo1173
- 1508 Van Weverberg, K., Morcrette, C. J., Petch, J., Klein, S. A., Ma, H.-Y., Zhang,
1509 C., ... Thieman, M. M. (2018). Causes: Attribution of surface radia-
1510 tion biases in nwp and climate models near the u.s. southern great plains.
1511 *Journal of Geophysical Research: Atmospheres*, n/a-n/a. Retrieved from
1512 <http://dx.doi.org/10.1002/2017JD027188> (2017JD027188) doi:
1513 10.1002/2017JD027188
- 1514 Vignon, E. (2017). *The extreme atmospheric boundary layer over the Antarctic*
1515 *Plateau and its representation in climate models* (Unpublished doctoral disser-
1516 tation). Université Grenoble-Alpes, (Grenoble, France).
- 1517 Vignon, E., Hourdin, F., Genthon, C., Gallée, H., Bazile, E., Lefebvre, M.-P., ...
1518 Van de Wiel, B. J. H. (2017). Parametrization of the boundary layer over
1519 the Antarctic plateau in a general circulation model: 1D simulations against
1520 summertime observations at Dome C. *J Geophys Res Atmos*, 122. (doi:
1521 10.1002/2017JD026802)
- 1522 Vignon, E., Hourdin, F., Genthon, C., Galle, H., Bazile, E., Lefebvre, M.-P., ...
1523 VandeWiel, B. J. H. (2017). Antarctic boundary layer parametrization in
1524 a general circulation model: 1-d simulations facing summer observations at
1525 dome c. *Journal of Geophysical Research: Atmospheres*, 122(13), 6818-6843.
1526 Retrieved from [https://agupubs.onlinelibrary.wiley.com/doi/abs/](https://agupubs.onlinelibrary.wiley.com/doi/abs/10.1002/2017JD026802)
1527 10.1002/2017JD026802 doi: 10.1002/2017JD026802
- 1528 Vignon, E., Hourdin, F., Genthon, C., Van de Wiel, B. J. H., Gallée, H., Madeleine,
1529 J.-B., & Beaumet, J. (2018). Modeling the dynamics of the atmo-
1530 spheric boundary layer over the Antarctic Plateau with a general circu-
1531 lation model. *Journal of Advances in Model Earth Systems*, 10, 98-125.
1532 (10.1002/2017MS001184)
- 1533 Vignon, E., van de Wiel, B. J. H., van Hooijdonk, I. G. S., Genthon, C., van der
1534 Linden, S. J. A., van Hooft, J. A., ... Casasanta, G. (2017). Stable bound-
1535 ary layer regimes at Dome C, Antarctica: observation and analysis. *Q J R*
1536 *Meteorol Soc*, 143(704), 1241-1253. (doi:10.1002/qj.2998)
- 1537 Vonder Haar, T. H., Bytheway, J. L., & Forsythe, J. M. (2012). Weather and cli-
1538 mate analyses using improved global water vapor observations. *Geophysical*
1539 *Research Letters*, 39(15). Retrieved from [https://agupubs.onlinelibrary](https://agupubs.onlinelibrary.wiley.com/doi/abs/10.1029/2012GL052094)
1540 [.wiley.com/doi/abs/10.1029/2012GL052094](https://agupubs.onlinelibrary.wiley.com/doi/abs/10.1029/2012GL052094) doi: 10.1029/2012GL052094
- 1541 Vuichard, N., Messina, P., Luyssaert, S., Guenet, B., Zaehle, S., Ghattas, J., ...
1542 Peylin, P. (2019). Accounting for carbon and nitrogen interactions in the
1543 global terrestrial ecosystem model orchidee (trunk version, rev 4999): multi-
1544 scale evaluation of gross primary production. *Geoscientific Model Develop-*
1545 *ment*, 12(11), 4751-4779.
- 1546 Wang, F., Cheruy, F., & Dufresne, J.-L. (2016). The improvement of soil
1547 thermodynamics and its effects on land surface meteorology in the ipsl
1548 climate model. *Geoscientific Model Development*, 9(1), 363-381. Re-
1549 trieved from <https://www.geosci-model-dev.net/9/363/2016/> doi:
1550 10.5194/gmd-9-363-2016
- 1551 Wang, F., Ducharne, A., Cheruy, F., Lo, M.-H., & Grandpeix, J.-Y. (2018).
1552 Impact of a shallow groundwater table on the global water cycle in the

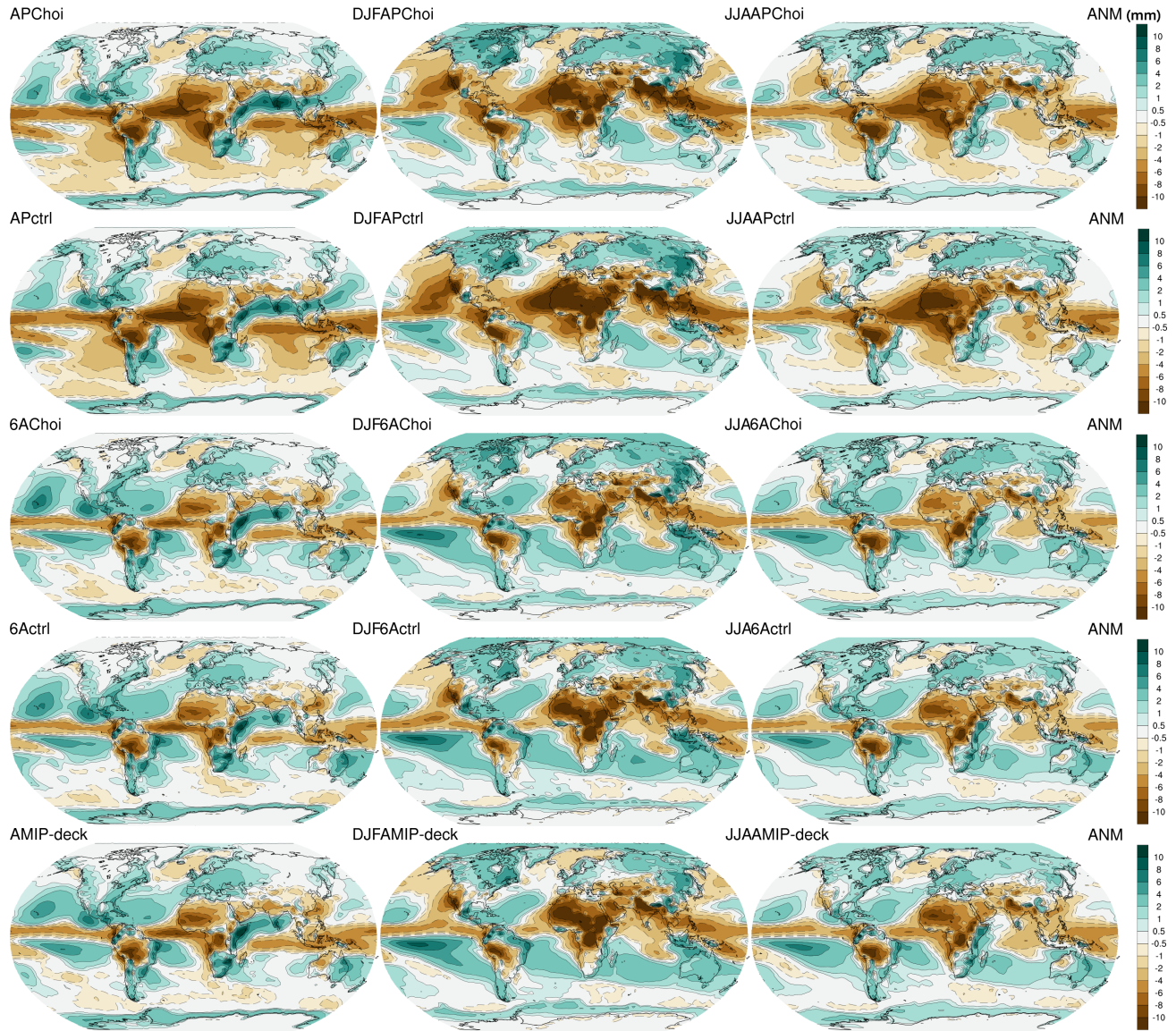
- 1553 ipsl land–atmosphere coupled model. *Climate Dynamics*, 3505–3522.
 1554 Retrieved from <https://doi.org/10.1007/s00382-017-3820-9> doi:
 1555 10.1007/s00382-017-3820-9
- 1556 Wang, T., Ottlé, C., Boone, A., Ciais, P., Brun, E., Morin, S., . . . Peng, S. (2013).
 1557 Evaluation of an improved intermediate complexity snow scheme in the
 1558 orchidee land surface model. *Journal of Geophysical Research: Atmo-*
 1559 *spheres*, 118(12), 6064–6079. Retrieved from <http://dx.doi.org/10.1002/>
 1560 [jgrd.50395](http://dx.doi.org/10.1002/jgrd.50395) doi: 10.1002/jgrd.50395
- 1561 Wei, N., Zhou, L., & Dai, Y. (2017). Evaluation of simulated climatological di-
 1562 urnal temperature range in cmip5 models from the perspective of plane-
 1563 tary boundary layer turbulent mixing. *Climate Dynamics*(49), 1,22. doi:
 1564 10.1007/s00382-016-3323-0
- 1565 Williams, C. J. R., Allan, R. P., & Kniveton, D. R. (2012, oct). Diagnosing atmo-
 1566 sphere–land feedbacks in CMIP5 climate models. *Environmental Research Let-*
 1567 *ters*, 7(4), 044003. Retrieved from [https://doi.org/10.1088/1748-9326/](https://doi.org/10.1088/1748-9326/7/4/044003)
 1568 [2F7%2F4%2F044003](https://doi.org/10.1088/1748-9326/7/4/044003) doi: 10.1088/1748-9326/7/4/044003
- 1569 Xie, S., McCoy, R., & Kein, S. . C. (2010). Clouds and more: Arm climate model-
 1570 ing best estimate data: A new data product for climate studies. *Bulletin of the*
 1571 *American Meteorological Society*, 91, 13,20.
- 1572 Yamada, T. (1983). Simulations of nocturnal drainage flows by a q^2l turbulence clo-
 1573 sure model. *J. Atmos. Sci.*, 40, 91-106.
- 1574 Zeng, Z., Piao, S., Li, L. Z., Zhou, L., Ciais, P., Wang, T., . . . others (2017). Cli-
 1575 mate mitigation from vegetation biophysical feedbacks during the past three
 1576 decades. *Nature Climate Change*, 7(6), 432–436.
- 1577 Zobler, L. (1986). *A world soil file for global climate modeling*. National
 1578 Aeronautics and Space Administration, Goddard Space Flight Center, In-
 1579 stitute for Space Studies. Retrieved from [https://books.google.fr/](https://books.google.fr/books?id=iMQ9ygAACAAJ)
 1580 [books?id=iMQ9ygAACAAJ](https://books.google.fr/books?id=iMQ9ygAACAAJ)











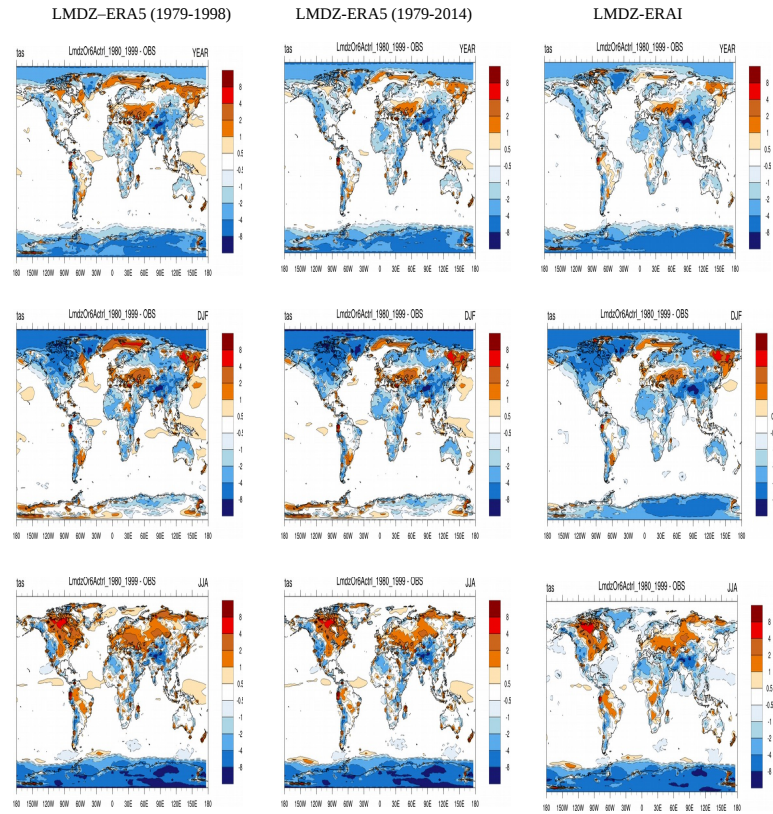


Figure S1. shows the maps of the annual (first row), DJF (second row) and JJA (last row) bias for 2m-temperature calculated for the 6Actrl version. The reference for the observations are (first column) ERA5(1979-1998), (second column) ERA5 (1979-2014), (third column) ERA-Interim (1979-1998)

